RSC Advances

PAPER

View Article Online
View Journal | View Issue

Cite this: *RSC Adv.*, 2018, **8**, 14377

Characterization of aluminum, aluminum oxide and titanium dioxide nanomaterials using a combination of methods for particle surface and size analysis†

B. Krause, *[a] T. Meyer,[b] H. Sieg,[c] C. Kästner, [d] P. Reichardt,[a] J. Tentschert,[a] H. Jungnickel,[a] I. Estrela-Lopis,[b] A. Burel,[e] S. Chevance, [f] F. Gauffre, [f] P. Jalili,[g] J. Meijer,[h] L. Böhmert,[c] A. Braeuning,[c] A. F. Thünemann, [d] F. Emmerling, [i] V. Fessard,[g] P. Laux, [a] A. Lampen[c] and A. Luch [a]

The application of appropriate analytical techniques is essential for nanomaterial (NM) characterization. In this study, we compared different analytical techniques for NM analysis. Regarding possible adverse health effects, ionic and particulate NM effects have to be taken into account. As NMs behave quite differently in physiological media, special attention was paid to techniques which are able to determine the biosolubility and complexation behavior of NMs. Representative NMs of similar size were selected: aluminum (Al^0) and aluminum oxide (Al_2O_3), to compare the behavior of metal and metal oxides. In addition, titanium dioxide (TiO_2) was investigated. Characterization techniques such as dynamic light scattering (DLS) and nanoparticle tracking analysis (NTA) were evaluated with respect to their suitability for fast characterization of nanoparticle dispersions regarding a particle's hydrodynamic diameter and size distribution. By application of inductively coupled plasma mass spectrometry in the single particle mode (SP-ICP-MS), individual nanoparticles were quantified and characterized regarding their size. SP-ICP-MS measurements were correlated with the information gained using other characterization techniques, *i.e.* transmission electron microscopy (TEM) and small angle X-ray scattering (SAXS). The particle surface as an important descriptor of NMs was analyzed by X-ray diffraction (XRD). NM impurities and their co-localization with biomolecules were determined by ion beam microscopy (IBM) and confocal Raman microscopy (CRM). We conclude advantages and disadvantages of the different techniques applied and suggest options for their complementation. Thus, this paper may serve as a practical guide to particle characterization techniques.

Received 8th January 2018
Accepted 22nd March 2018

DOI: 10.1039/c8ra00205c

rsc.li/rsc-advances

Introduction

The specific properties of NMs depend on their physicochemical characteristics. Optical properties build upon the size, the shape and the surface structure,[1,2] while higher reactivity, for example, may result from a high surface area,[3,4] specific surface coatings[5] or a surface charge.[6–8] An important factor for increasing their activity is the self-assembly of NMs. Here, NMs associate *via* non-covalent interactions resulting in organized structures of higher-order. Different applications based on advanced functions were

[a]*German Federal Institute for Risk Assessment (BfR), Department of Chemical and Product Safety, Max-Dohrn-Straße 8-10, 10589 Berlin, Germany. E-mail: benjamin-christoph.krause@bfr.bund.de*

[b]*Institute of Medical Physics and Biophysics, University of Leipzig, Härtelstrasse 16-18, 04275 Leipzig, Germany*

[c]*German Federal Institute for Risk Assessment (BfR), Department of Food Safety, Max-Dohrn-Straße 8-10, 10589 Berlin, Germany*

[d]*Federal Institute for Materials Research and Testing (BAM), Unter den Eichen 87, 12205 Berlin, Germany*

[e]*MRIC TEM BIOSIT, Université de Rennes 1, 2 av pro Leon Bernard, France*

[f]*Univ Rennes, CNRS, ISCR UMR6226, F-35000 Rennes, France*

[g]*ANSES, French Agency for Food, Environmental and Occupational Health and Safety, Fougères Laboratory, 10B rue Claude Bourgelat, 35306, Fougères Cedex, France*

[h]*Felix Bloch Institute for Solid State Physics, Faculty of Physics and Geosciences, Division of Nuclear Solid State Physics, University of Leipzig, Linnéstraße 5, 04103 Leipzig, Germany*

[i]*Federal Institute for Materials Research and Testing (BAM), Richard-Willstätter-Straße 11, 12489 Berlin, Germany*

† Electronic supplementary information (ESI) available: NTA size distributions for Al^0, Al_2O_3, NM103, NM104, DLS number-based distribution for Al^0, Al_2O_3, NM103, NM104, TEM measurement of TiO_2 NMs in DMEM, SAXS data for Al^0, Al_2O_3 and $AlCl_3$ in BSA and DMEM after 24 and 48 h, impurities of used NMs determined by IBM, aluminium aqua complexes at different pH values, CRM surface investigations, colocalization pattern by IBM for Al_2O_3, CRM spectra displaying protein modifications, ToF-SIMS measurements of Al and Al_2O_3 NMs in DMEM, ToF-SIMS measurements of TiO_2 NMs in DMEM. See DOI: 10.1039/c8ra00205c

reported, for example formation of mesoporous TiO_2 mediated by ionic liquids for solar cell conversion, catalysis or electronic devices.[9–11] Another application is the self-assembly of biomolecules, like lipids and proteins, mediating inner-particle mesoporosity in a macroporous TiO_2 structure.[12]

TiO_2 NMs are classified as granular biodurable particles (GBPs) of low toxicity.[13] They occur in the form of anatase or rutile as well as in mixtures thereof. While significant accumulation was shown in the liver of rats in the case of orally administered TiO_2 NMs,[14] this was different in studies with Al^0 NMs in mice, in which predominant accumulation in the brain, thymus and lung was revealed.[15] Characterization is important for both *in vitro* and *in vivo* studies. Currently, the human health risk assessment of NMs is mainly based on *in vivo* experiments in rodents.[16,17] However, due to the high number of new NMs,[18] it is not ethical or feasible to conduct such studies for each individual NM. On the other hand, *in vitro* systems proved useful, *e.g.* to generate high throughput data.[19] Extrapolation to the *in vivo* situation remains limited, in particular due to the insufficient comparability of applied dose and particle biotransformation.[20,21] An accurate characterization of NMs in *in vitro* systems by the application of up-to-date analytical methods may therefore help to establish reliable methods for determination of nanomaterial uptake and translocation as key parameters that affect NM-related toxicity. Such an approach would therefore help to reduce the number of materials that need to be subjected to animal testing. We investigated rather soluble Al^0 and rather insoluble Al_2O_3 and TiO_2 NMs (Fig. 1).

This classification is important for NMs because even the same chemical composition can exhibit differences in physicochemical properties. Compared to bulk material, variations are much higher for NMs.[22,23]

For the characterization of test materials, we applied a combination of techniques based on different measuring principles. With DLS as intensity-weighted method, we assessed the hydrodynamic diameter and the polydispersity of the materials in aqueous suspensions and cell culture media (CCM). To validate the results, the more reliable, number-based approach of NTA was applied. The two methods, DLS and NTA, were performed in two different laboratories, allowing for a direct comparison of the results achieved. For particle surface investigation, XRD was used to test whether the aluminum was already oxidized. The core diameter of Al^0, Al_2O_3 and both TiO_2 NMs was measured by SP-ICP-MS. These results were compared to TEM measurements. As a further technique for estimation of the core diameter, SAXS was applied. Additionally, IBM and CRM were performed to analyze the interaction of NMs with biomolecules as well as to quantify impurities in the NM composition. ToF-SIMS is capable of visualizing the formation of complexes out of Al^0 and Al_2O_3 NMs with components of the environmental media. This allows investigation of the behavior of NMs within physiological fluids such as CCM.

With respect to uptake, the dissolution of NMs in different media is of high importance. For example, during an artificial digestion procedure, different pH values, as well as proteins, enzymes and other compounds, mimic the oral uptake route for NMs. For Al^0 and Al_2O_3 NMs, an increased dissolution within the gastric environment was noticed.[24] However, to properly interpret and compare the results, precise knowledge of the properties of the starting materials and of their state in CCM is required. Although there are a lot of studies dealing with silver and copper-containing NMs and their dissolution behavior in biological media,[25–27] to our knowledge, no study accounts for Al^0 NMs. Furthermore, the dissolution behavior of aluminum-containing nanomaterials may be very different since aluminum ions already have a different complexation behavior compared to silver or copper ions. By means of the methods described earlier (Fig. 2), we were able to obtain valuable information to hypothesize the behavior of NMs in biological media and to extrapolate to the *in vivo* situation. With these assumptions, it is much easier to understand and explain future data resulting from more complex scenarios.

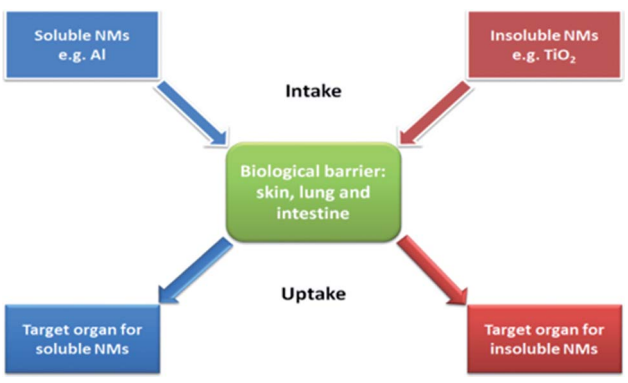

Fig. 1 Hypothesis of different behavior of soluble and insoluble NMs after uptake.

Experimental

Materials and methods

Al^0 NMs (mean diameter 18 nm (TEM), 99.9%) and Al_2O_3 NMs (mean diameter 20 nm (TEM), 99+%) were purchased from IoLiTec Ionic Liquids Technologies GmbH, Heilbronn, Germany. TiO_2 NMs (NM103 and NM104, mean diameter 25 nm (TEM)) were purchased from JRC Joint Research Centre, Ispra, Italy. Bovine serum albumin (BSA) was bought from Sigma Aldrich. CCM (DMEM, high glucose (4.5 g l^{-1}), with sodium pyruvate; with L-glutamine; with 1% penicillin/streptomycin (P/S)) and fetal bovine serum were purchased from PAA Laboratories GmbH, Paching, Austria. All other chemicals used in this study were reagent grade.

Sample preparation

NM dispersions were prepared following the NanoGenoTOX dispersion protocol "Final protocol for producing suitable manufactured NMs exposure media" (October 2011).[28]

For cell culture experiments, stock dispersions of NMs were diluted in DMEM with 10% fetal calf serum (FCS) to either 10 or 100 μg ml^{-1}.

For ion release testing, stock dispersions were diluted in 0.05% BSA to 100 and 10 μg ml^{-1} to reflect a high and a low

concentration used in cell culture experiments. 1 ml was taken and centrifuged at 16000 × *g* for 1 h (Hettich Zentrifuge Mikro 220R). 500 µl of the supernatant were taken, 750 µl of HNO_3 (69%) were added and Millipore water was used to fill up to 15 ml.

For IBM and CRM, NMs were centrifuged at 8000 × *g* for 10 min, supernatant was taken away, mpH_2O was added and the sample was vortexed. The procedure was repeated 3 times. Finally, a small drop of the sample was given on polypropylene foil for IBM and on quartz glass for CRM. The dry samples were measured.

Dynamic light scattering measurements

The distributions of the hydrodynamic diameters of the NMs were determined using a Malvern Nano ZS (Malvern Inc., UK) or a Brookhaven ZetaPALS (Brookhaven Instruments Corporation, USA). A stock dispersion (2.56 mg ml^{-1} in 0.05% BSA) was diluted to the concentration of 100 µg ml^{-1}. The NM dispersions in 0.05% BSA as well as in DMEM were analyzed 5–10 min after preparation. Thermal equilibration time was set to 60 s at 25 °C. Each intensity-weighted size distribution represents the average of six individual DLS analyses, three replicates and at least three independent experiments using automatic optimization of analytical conditions and data treatment by general purpose size analysis.

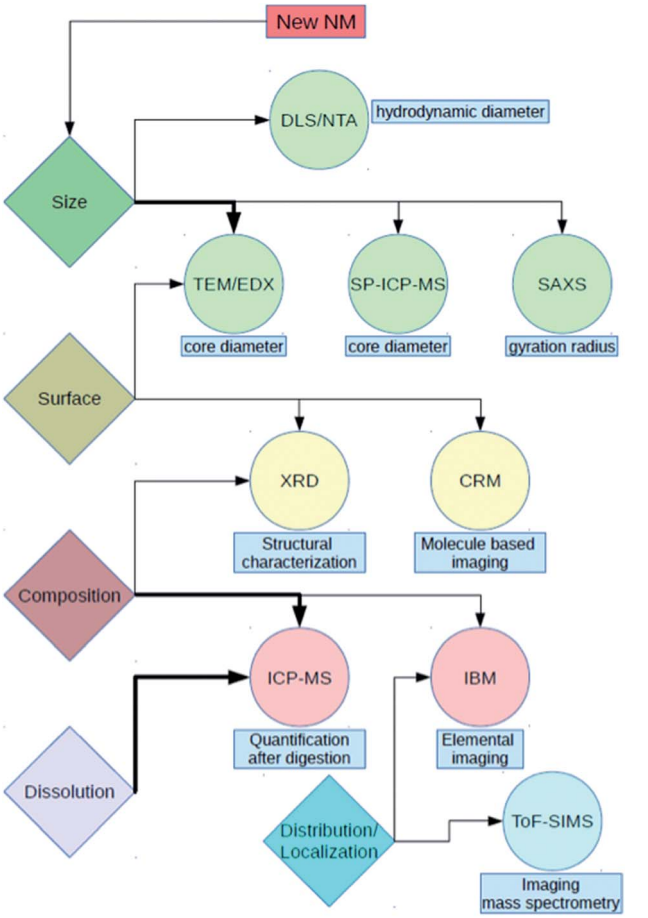

Fig. 2 Overview of key NM characteristics (colored rhombi) and methods (colored circles) used in this study for characterization. Arrows in bold imply the main method for the linked characteristic. Abbreviations: DLS – dynamic light scattering; NTA – nanoparticle tracking analysis; TEM – transmission electron microscopy; EDX – energy dispersive X-ray spectroscopy; SP-ICP-MS – single particle inductively coupled plasma mass spectrometry; SAXS – small angle X-ray scattering; XRD – X-ray diffraction; CRM – confocal Raman microscopy; ICP-MS – inductively coupled plasma mass spectrometry; IBM – ion beam microscopy; ToF-SIMS – time of flight mass spectrometry.

Nanoparticle tracking analysis measurements

NTA measurements were performed with a NanoSight LM20 and LM10 (NanoSight, Amesbury, UK), equipped with a 632 nm laser or 532 nm laser. The samples were injected into the sample chamber with sterile syringes. All measurements were performed at room temperature. The samples were diluted to a final concentration of approx. 10^8 particles per ml with mpH_2O, depending on the NMs and media. The software used for recording and analyzing the data was NTA 2.3 and NTA 3.0. All samples were measured for 60 s at five positions. All measurements were performed with at least three independent experiments.

X-ray diffraction measurements

The XRD measurements were achieved on powder samples using a D5000 diffractometer (Siemens AG, Munich, Germany) in Bragg Brentano geometry. A linear detector, a curved Ge(111) monochromator and Cu K_α radiation (λ = 0.1542 nm) were used. The analysis was performed over the 2θ range of 10 to 90° and at a step size of 0.02° and scanning speed of 2° per step. The experiments were carried out independently three times.

Single particle ICP-MS measurements

For single particle analysis of the NM solutions, a quadrupole ICP-MS (Thermo Scientific XSERIES II, Thermo Fisher Scientific, Waltham, MA, USA) with a PFA ST Nebulizer, a quartz cyclonic spray chamber and a 2.5 mm quartz O-ring-free injector (all from ESI Elemental Service & Instruments GmbH, Mainz, Germany) were used. Using the time-resolved analysis (TRA) mode for data acquisition, intensities as a function of time (counts per dwell-time interval) were collected. The acquisition time for each run was set to 60 s with a dwell time (or data acquisition rate) of 3 ms. The gas flow for the plasma, the nebulizer and the auxiliary (all Ar) was set to 13 l min^{-1}, 0.89 l min^{-1} and 0.7 l min^{-1} respectively. The flow rate of the sample was 0.34 ml min^{-1}. Data were exported to a spreadsheet for further processing. For data processing, an established procedure according to Pace *et al.*[29] was followed. Determination of nebulizer efficiency was performed using a described method with reference nanoparticles of known particle size.[29] 60 nm gold reference nanoparticles from the U.S. National Institute of Standards and Technology (NIST, RM 8013) were used as reference nanoparticles.

Small angle X-ray scattering measurements

The measurements were conducted in a flow-through capillary with a Kratky-type instrument (SAXSess, Anton Paar, Austria) at 21 ± 1 °C. The SAXSess has a low sample-detector distance of 0.309 m. Deconvolution of the SAXS curves was carried out with the SAXS-Quant software. Curve fitting was performed with the McSAS software (Monte Carlo method, version 1.0.1). The experiments were performed with 120 measurement cycles (each averaged over 10 s). NMs and controls were dispersed according to NanoGenoTOX protocol and diluted into DMEM in a sample concentration of 100 μg ml^{-1}. Samples were incubated for a time of 24 and 48 h at 37 °C and 5% CO_2 in a cell incubator until sample injection. Stock dispersions were injected directly after ultrasonication.

Ion beam microscopy

Label-free IBM measurements were performed with the LIPSION Nanoprobe. A 2.25 MeV proton beam was applied by a Singletron™ particle accelerator. A vacuum with a pressure of 5×10^{-5} to 10^{-7} torr was applied and the beam was focused to a spot size of around 1 μm. For spatial resolved element analysis, micro proton induced X-ray emission (μPIXE) and micro Rutherford backscattering spectroscopy (μRBS) were recorded simultaneously. The μPIXE detector (Canberra, Meriden, CT, USA) consists of a high-purity Ge crystal covered with a 60 μm polyethylene layer, which covers the detector for backscattered protons. μRBS spectra were detected by a Canberra PIPS detector.

Confocal Raman microscopy

Spectroscopic analysis of NMs was performed by CRM. A Witec alpha300 confocal Raman spectrometer (Witec GmbH, Germany) with a 532 nm laser with 30 mW power was used. Control4.1 (Witec GmbH, Germany) software was used to record and analyze the spectra. The spectra were recorded at an integration time of 0.15 s per point and with a step size of 250 nm.

Transmission electron microscopy

The samples were deposited on a 400-mesh copper grid. The grids were prepared by sample adsorption and left free-standing on top of a 0.8 mg ml^{-1} solution of NMs for 20 s. Excess solution was removed by placing the grid on a filter paper and the sample was dried for 24 h. For samples in DMEM, the grid was washed by dipping the grid in a droplet of water before. Examination was performed with a JEOL 1400 transmission electron microscope, equipped with a tungsten filament and supplied with GATAN Orius 1000 camera. TEM operated at 80 kV (DMEM) or at 120 kV with magnification of 200 000×.

Time-of-flight mass spectrometry

Ion images and spectra were acquired using a ToF-SIMS V instrument (ION-TOF GmbH, Münster, Germany) with a 30 keV nano-bismuth primary ion beam source ($[Bi]x^{(y+)}$-cluster ion source with a BiMn emitter). The ion currents were 0.5 pA at 5 kHz using a Faraday cup. A pulse of 0.7 ns from the bunching system resulted in a mass resolution that usually exceeded 6000 (full width at half-maximum) at $m/z < 500$ in positive ion mode. The primary ion dose was controlled below 1012 ions cm^{-2} to ensure static SIMS conditions. Charge compensation on the sample was obtained by a pulsed electron flood gun with 20 eV electrons.

The primary ion gun scanned a field of view of 500 μm × 500 μm applying a 512 × 512 pixel measurement raster. Once the primary ion gun was aligned, a ToF-SIMS mass spectrum was generated by summing the detected secondary ion intensities and plotting them against the mass channels. The data were evaluated using the Surface Lab software (ION-TOF GmbH, Münster, Germany).

Results and discussion

We point to the advantages and disadvantages of the methods used and explain whether or not methods can provide complementary results to other techniques. We also analyzed possible dissolution characteristics of different matrix media (BSA and DMEM) for pristine Al^0 and oxide (Al_2O_3 and TiO_2) NMs. Characterization data already published on TiO_2 were retrieved according to JRC report.[30] In conclusion, we will present data where the dissolution of NMs in complex media has an impact on particle media interactions. These results were obtained by ToF-SIMS and show the efficiency of that method for obtaining insights into elemental compositions with TEM, IBM, CRM and ToF-SIMS. An overview about the main characterization techniques and their limits is given in Table 3.

A very common and frequently used method for determining the size distribution and polydispersity of NMs in solution is DLS. Fast and easy sample preparation as well as quick measurement give rapid initial indications of the sample. NTA is more appropriate for evaluating polydisperse samples with

Table 1 *Z*-averages with standard deviation (SD) and polydispersity index (PDI) of Al^0, Al_2O_3, NM103 and NM104 NMs in different media determined by dynamic light scattering (DLS). All results represent the average of six repeats. BSA: bovine serum albumin; DMEM: Dulbecco's modified eagle medium; FCS: fetal calf serum

DLS measurements and comparison				
	Lab 1 (Malvern)		Lab 2 (Brookhaven)	
	Z-average [nm]	PDI	*Z*-average [nm]	PDI
Stock solution (0.05% BSA in H_2O)				
Al^0 NM	250 ± 10	0.17 ± 0.01	270 ± 40	0.18 ± 0.02
Al_2O_3 NM	170 ± 10	0.24 ± 0.02	210 ± 40	0.21 ± 0.06
NM103	270 ± 10	0.28 ± 0.05	610 ± 190	0.21 ± 0.30
NM104	220 ± 10	0.26 ± 0.03	370 ± 90	0.15 ± 0.03
DMEM (with 10% FCS)				
Al^0 NM	200 ± 10	0.18 ± 0.01	220 ± 10	0.21 ± 0.02
Al_2O_3 NM	70 ± 10	0.52 ± 0.03	230 ± 60	0.18 ± 0.07
NM103	240 ± 20	0.24 ± 0.01	270 ± 10	0.25 ± 0.01
NM104	190 ± 10	0.28 ± 0.02	230 ± 10	0.18 ± 0.02

various aggregate populations, since it is based on single particle tracking as both techniques determine the hydrodynamic diameter. Due to the fixed working ranges of DLS and NTA, the used concentration of media various. Since NTA is a counting method, also proteins would be counted and would significantly lower the hydrodynamic diameter of the NM dispersion. Therefore, the particles, as well as the medium were diluted directly before measurement with mpH_2O to avoid agglomeration effects.

For all particles with a primary size of approximately 20 nm, a hydrodynamic diameter between 200 and 270 nm was measured by DLS in DMEM (Table 1). In contrast, different aggregate fractions of NMs in DMEM with a mean value of about 150 nm were found by means of NTA (Fig. S1†). This difference can be explained by the fact that NTA is a particle counting system, sensitive to large as well as small fractions in the sample, and DLS is an intensity-weighted system, highly responsive to the large fractions. In all cases, the NTA size distribution is asymmetrical with a steep slope on the left side (small particles) and a gentle slope on the right side, representing the fraction of agglomerates. Additionally, a calculation of number-based size distribution out of intensity-weighted DLS data was done (Table S1†).

In the case of NM103 and NM104 dispersed in 0.05% BSA water solution, a very high mean value and a large error was measured by the Brookhaven device, while NTA exhibits broad distributions with some fractions and a mean value of around 180 nm. This can be explained by unstable particle agglomerates, which are observed by the DLS.

Comparing the two DLS devices, one can observe that the Malvern DLS detects 15% smaller particles than the Brookhaven machine in 0.05% BSA water solution as well as in DMEM. This systematic deviation could be related to different detection angles of scattered intensity, 90° for Brookhaven and 173° for Malvern, since larger particles mostly scatter light at forward angles. Backscattering at 173° will not overestimate larger particles as much as measurements at 90°.

In the case of NM103 and 104 in BSA and Al_2O_3 in DMEM, the results were not consistent for the two devices. *Z*-averaged diffusion coefficients were calculated by applying the cumulant method, which is applicable to polydisperse and non-multimodal systems. In contrast, NTA results show the presence of different particle populations. The applied cumulant algorithms are not suitable in certain cases for getting reliable DLS results. Furthermore, it should be kept in mind that the inversion of the DLS autocorrelation function is part of a poorly formulated mathematical problem. It works quite well in the case of monodisperse or low polydisperse particles. Applications of multiangle DLS and sophisticated algorithms are thus necessary to obtain trustworthy results of NM size distributions by means of DLS.[31,32]

Investigations on primary particle size

With the European commission's definition of a nanomaterial, that is, a nanomaterial should contain 50% or more particles in number size distribution with one or more size dimensions between 1–100 nm, it is obviously necessary to obtain information about the primary particle size of the investigated particles. TEM as well as SAXS can be used to solve this problem.

Looking at advantages and disadvantages of TEM, the following issues should be considered. Since TEM measurements are performed under high vacuum, only dried samples are observed. For this reason, TEM is not representative of the sample in its solution state. In particular, agglomeration and coffee stain effect[33] may occur during the drying process, resulting in a non-homogenously covered surface. Size distributions can be determined from TEM pictures by measuring the size of each particle using image analysis software.[34] The size of individual nanoparticles may be difficult to extract from agglomerated samples but, recently, some implementations have been proposed.[35] In addition, for irregular particles with ill-defined shapes, which dimension should be taken? In practice, size analysis can be time-consuming and TEM generally yields a poor statistical representation of the sample.[34] Electron microscopy also enables chemical and crystallographic analysis of the particles. The contrast in TEM is directly linked to the atomic number of electrons, heavier atoms giving higher contrast. This is an advantage when observing metal nanoparticles in a biological environment. However, care should be taken for mineral salts from buffers that may precipitate on the grid when drying. Aqueous washing of the grid after sample deposition might be appropriate in this case.

Fig. 3 shows the dispersion in water with 10% BSA. The shape of Al^0 NMs is globally spherical with rod-like excrescences and the primary particle size varies between 2–50 nm, which matches the manufacturer specification. The Al_2O_3 NMs are not spherical but have rather a needle-like shape. The width is about 10 nm, while the longest dimension varies a bit more between 20–50 nm. The shape of TiO_2 NM104 is rod-like, with a width of approx. 10 nm and length of 20–50 nm (Fig. S2†). Working with a more complex medium, such as CCM, was challenging for TEM analysis. However, we were able to image the particle in DMEM, with very little differences compared to BSA dispersion. Using relatively low voltage, the protein coating can be observed (see Fig. S2†).

SAXS was used for characterization of the primary particle size of NMs. SAXS allows to analyze a broader variety of different sample types than most other techniques. Compared to TEM, the samples can easily be investigated *in situ*. Additionally, SAXS provides statistically more reliable data for particle size distribution quantification since more than 10^6 particles are typically measured, in contrast to TEM, where rarely more than a few

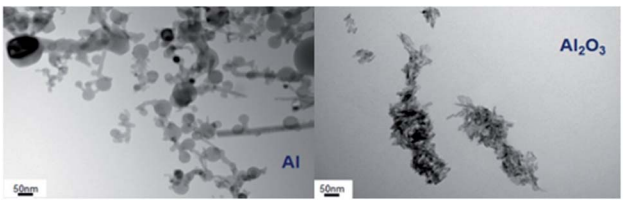

Fig. 3 Comparison of TEM pictures of Al^0 and Al_2O_3 NMs in BSA solution after applying the dispersion protocol.

hundred particles are counted. Size distribution of NMs can be quantified in the range of 1 to 100 nm if the shape is known from a complementary technique like TEM. The classical radius of gyration (Guinier radius) is accessible in any case.

In this study, we observed the size parameters of the particles in BSA as a stock solution and after addition in DMEM at different times of $t = 0$ h, 24 h and 48 h (Fig. 4). Since the particle cores scatter much stronger than the surrounding particle shell, the shell becomes practically invisible. Therefore, SAXS determines the size distribution of the core radii. The resulting distributions of the particles' stock solutions are shown in Fig. 4. Their corresponding SAXS curves are displayed in the ESI (Fig. S3–S5†). The accessible size range of the radii is given by the range of the scattering vector q: $R_{min} = \pi/q_{max}$ and $R_{max} = \pi/q_{min}$. In the present case of the q-range of 0.1 $nm^{-1} < q < 6$ nm^{-1} corresponds to radii of 30 nm > R > 0.5 nm.

The Al^0 NMs showed a broad size distribution including primary particles with radii > 10 nm. Since the detection limit is 30 nm (radius) in this case, bigger aggregates cannot be detected directly. However, from the steep slope of the SAXS curve (Fig. S3†) at low q values, it can be assumed that bigger aggregates are present. The defined characterization of these particle aggregates has to be performed using a complementary method like TEM. The inset in Fig. 4a shows that the radii distribution of the Al^0 NMs did not change significantly either after addition in DMEM or 24 h and 48 h thereafter. In contrast to the Al^0 NMs, the Al_2O_3 NM in BSA displays a distribution which consists of small primary particles and aggregates. The sample shows an amount of 75% primary particles with a mean radius of 7.1 ± 0.5 nm. The detected aggregates display radii of > 10 nm. Upon the addition in DMEM, the radii distribution shifts slightly to higher radii of 8.4 ± 0.2 nm. These characteristics did not change significantly over the time of 48 h in DMEM.

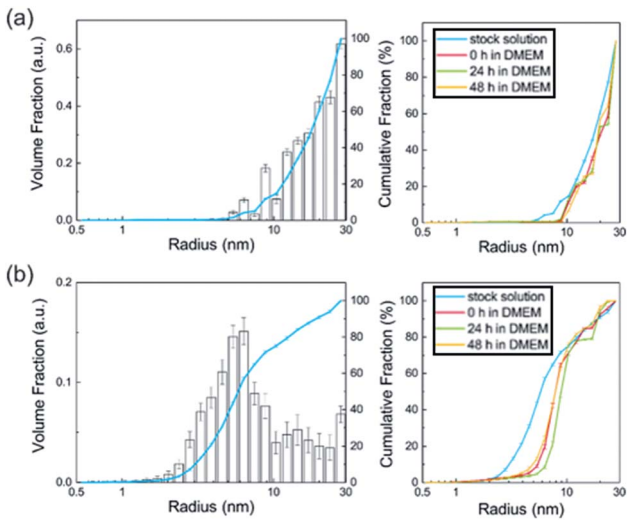

Fig. 4 Volume-weighted radii distributions of Al^0 NMs (a) and Al_2O_3 NMs (b) derived from SAXS measurements. The displayed radii distribution (right panel, black bars) and cumulative fraction presentation (blue line) correspond to the NMs in stock solution (BSA). Left panel shows particle distribution in cumulative fraction presentation at different stages: in stock solution (blue line) and in DMEM after 0 h (red line), 24 h (green line) and 48 h (orange line).

No particles were detected in the ionic control substance $AlCl_3$. In contrast, immediately after addition in DMEM, nano-scaled particles with sizes of 1–30 nm were observed. Since all curves are background-corrected with the respective solvent control, solvent effects can be excluded and the particles derive directly from the aluminum species. In conclusion, SAXS yields the size distribution of nanoparticles and its changes in DMEM.

SP-ICP-MS is another technique to determine primary particle sizes. The fundamental assumption behind this technique is that, at a sufficiently short dwell time and low particle number concentration, a pulse will represent a single particle event.

There is a direct correlation between the number of pulses and the number concentration of particles (particle number per volume). With the intensity of the pulse (*i.e.* height) and assumptions about the particle geometry, the particle size through particle mass can be determined.

Aside from single pulses, there is always a background, which originates from the ionic part of the analyzed sample. In addition to primary particle size, information about the dissolution rate of a NM sample can be achieved. While quantification is more difficult, a qualitative assessment of ions released can be inferred. For Al^0, a broad distribution (Fig. 5, left) up to 200 nm is observed compared to Al_2O_3 (Fig. 5, right). This fits very well with the data obtained from TEM analysis. Compared to the Au NIST reference material, which shows almost no dissolution, a higher background for Al^0 NMs was detected, indicating potential ion release.

Particle surface – impact on dissolution in complex media

Al^0 NMs usually become quickly passivated at the surface by the formation of an oxide layer. This event is likely to change the dissolution behavior and the overall physicochemical

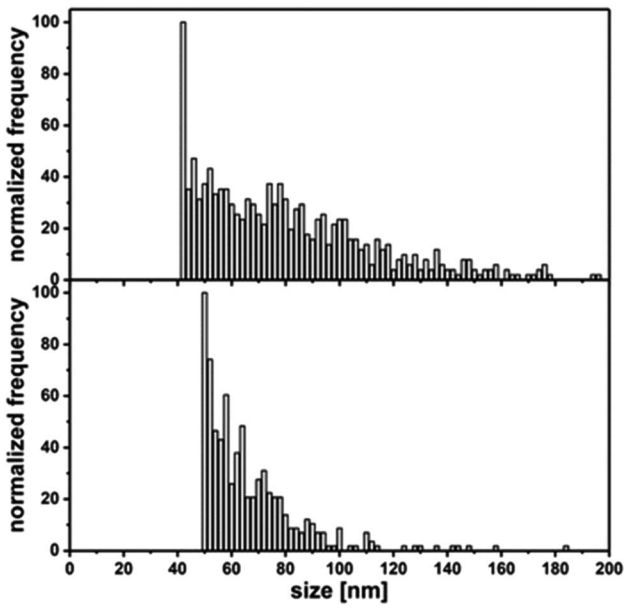

Fig. 5 Top: primary particle size distribution of Al^0 in 0.05% BSA determined by SP-ICP-MS; bottom: Primary particle size distribution of Al_2O_3 in 0.05% BSA determined by SP-ICP-MS.

characteristics of Al^0 NMs. For comparison, we also investigated Al_2O_3 particles of similar size. To prevent the surface oxidation of Al^0 NMs, its processing and handling in an inert gas atmosphere was evaluated.

Investigation by XRD revealed a thin aluminum oxide layer at the surface of the Al^0 NMs (Fig. 6, left). This was confirmed by TEM measurements and has also already been shown in the literature for another Al^0 NM by TEM measurements (2.5 nm oxide layer).[36] The occurrence of an oxide layer can be explained by partial passivation of the material due to manufacturer's processing.

In comparison with Al^0 NMs, the diffractogram of Al_2O_3 particles showed clear differences (Fig. 6, right). The diffractogram of Al^0 NMs showed a higher intensity for the aluminum peaks, *e.g.* at 38°, 45°, 66° and 78° (Fig. 6, left) as compared to Al_2O_3 peaks, *e.g.* at 37°, 46° and 67° (Fig. 6, right). This demonstrates that even though there is an Al oxide layer at the surface of the Al NMs they are not completely oxidized.

To confirm these results, we used electron energy loss spectroscopy (EELS). Here the sample becomes exposed to an electron beam with defined kinetic energy. Some electrons undergoing inelastic scattering are collected in a detector. The loss of energy reflects the chemical composition of the sample.

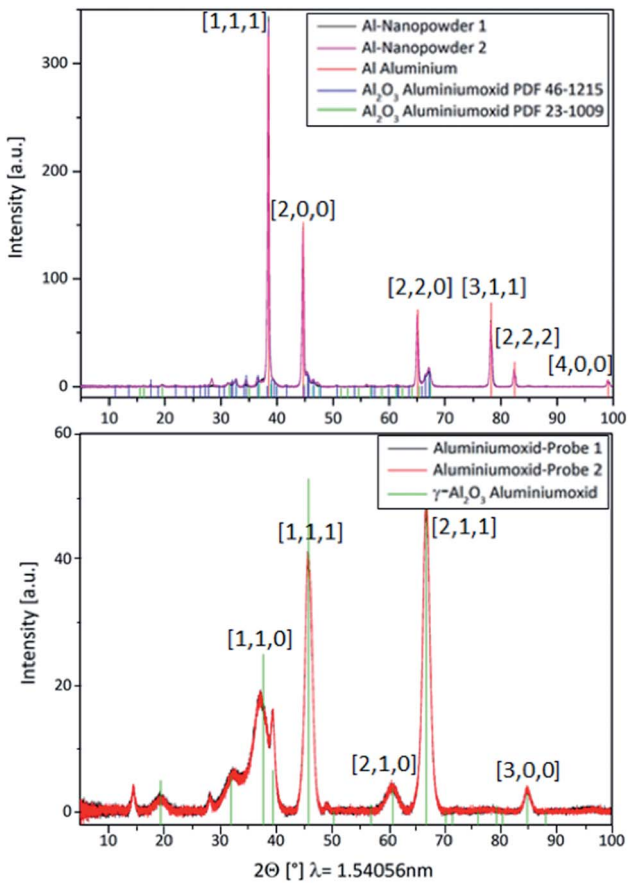

Fig. 6 Top: XR-diffractogram of Al^0 NMs red: database entry for Al; blue; (green: database entry for Al_2O_3), space group: *Fm3m*, lattice constants: $a = 4.0494$ Å; bottom: diffractogram of Al_2O_3 NMs (red: database entry for Al_2O_3), space group: *Fd3m*, lattice constants: $a = 7.906$ Å.

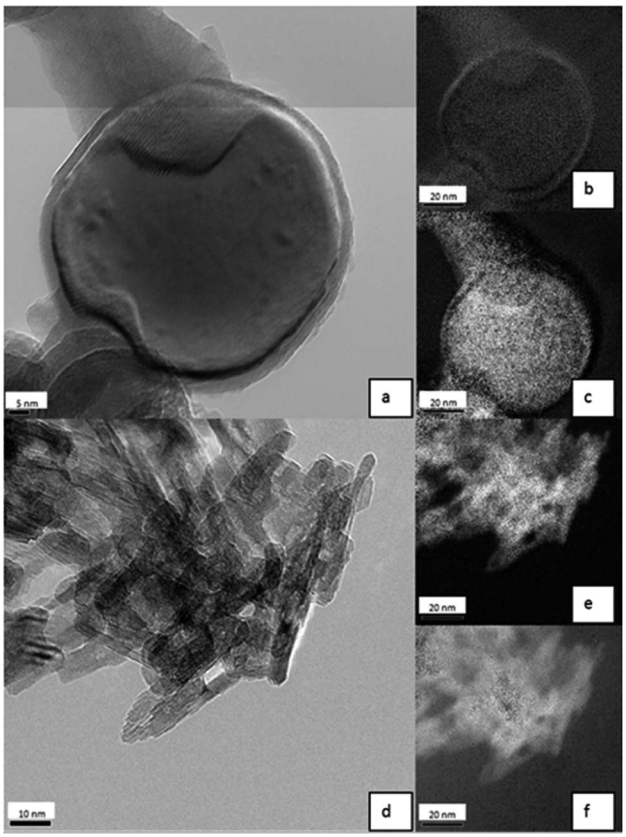

Fig. 7 (a): TEM picture of Al^0 NMs, 200 k magnification; (b) oxygen mapping of left TEM picture; (c) Aluminum mapping of left TEM picture. (d) TEM picture of Al_2O_3 NMs, 200 k magnification; (e) aluminum mapping of left TEM picture; (f) oxygen mapping of left TEM picture.

Analysis of Al^0 NMs in 0.05% BSA (Fig. 7a) revealed a core–shell structure. By means of EELS, it was proven that the shell is rich in oxygen (Fig. 7b), while the core consists of elemental aluminum (Fig. 7c). The TEM results indicate an oxide layer of about 2 to 5 nm.

Elemental mapping of Al_2O_3 NMs showed a quite different picture compared to pure Al^0 NMs (Fig. 7d). The distribution of aluminum and oxygen was homogenous over all NMs (Fig. 7e and f). These results show that Al_2O_3 NMs are fully oxidized while elemental Al^0 NMs were passivated by an oxide layer. It is

Table 2 Ion release of Al^0 and Al_2O_3 NMs compared to recovery of $AlCl_3$ in 0.05% BSA and DMEM

		Ion release in BSA [%]	Ion release in DMEM [%]
Al^0 NMs	10 μg ml^{-1}	0.4 ± 0.1	0.5 ± 0.1
	100 μg ml^{-1}	0.3 ± 0.1	0.4 ± 0.1
Al_2O_3 NMs	10 μg ml^{-1}	0.4 ± 0.1	1.4 ± 0.1
	100 μg ml^{-1}	0.2 ± 0.1	0.4 ± 0.1
$AlCl_3$	10 μg ml^{-1}	140 ± 9	112 ± 4
	100 μg ml^{-1}	94 ± 4	66 ± 3

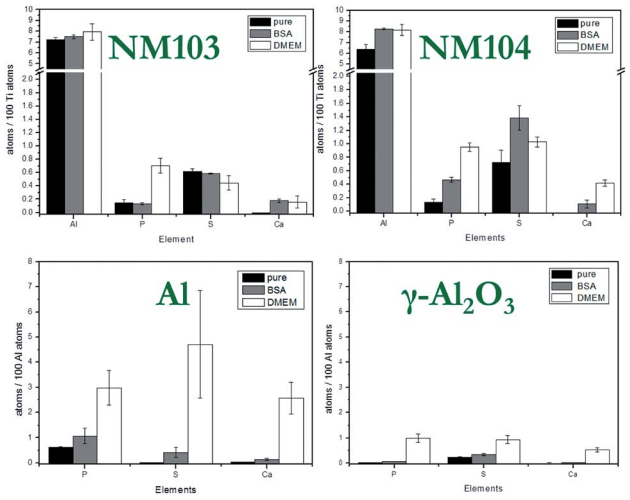

Fig. 8 IBM element analysis of NM103, NM104, Al and Al_2O_3 NMs. NMs as purchased and diluted in water (pure), NMs with albumin corona in H_2O (BSA) and NMs under cell exposure conditions (DMEM). The graph demonstrates the ratio of atoms of several elements compared to 100 atoms of titanium or aluminum.

also visible because Al^0 NMs are dark grey to black, while Al_2O_3 NMs are white.

The results from surface investigations *via* XRD and EELS suggest a different solubility of Al^0 compared to Al_2O_3. Indeed, the thin oxide layer on Al^0 allows the release of ions while the fully oxidized Al_2O_3 particle should be much more inert. Nevertheless, due to the highly specific surface, a higher solubility compared to Al_2O_3 bulk material could be expected as more potentially ion releasing Al atoms are present on the surface.

Influence of particle composition and impurity patterns

Compared to particle size and surface, the particle composition has a much higher impact on the solubility and dissolution behavior of NMs. One of the most widely used methods due to its high sensitivity, broad range for nearly all elements and detection limits down to the sub-ppb level is the ICP-MS. Unknown samples can be not only detected but also quantified. For more complex samples, microwave-assisted digestion prior to ICP-MS analysis could be performed. In this study, we confirmed the already known composition of the NMs by XRD and EELS measurements as well as ICP-MS analysis. For the assessment of particle toxicity, it is also important to take impurities into account which might alter ion release behavior. Due to element-specific μRBS and μPIXE, IBM became the method of choice for these investigations. The main impurities of aluminum-containing NMs were phosphorus, sulfur and chlorine, which could lead to a different ion release compared to pure materials (see Fig. S6†).

Solubility investigations on Al^0 and Al_2O_3 NMs

To verify our hypothesis that Al^0 NMs are more soluble than Al_2O_3, we performed ion release experiments in stock dispersions and DMEM. Adjusting the pH value was not necessary due to almost neutral pH values of 7.3 in stock dispersion compared to 7.2 in DMEM. Keeping in mind that aluminum is an amphoteric material due to the aluminum aqua complexes, one can assume that dissolution of Al^0 NMs in complex media is highly pH-dependent. Compared to an acid, the aluminum aqua complex reacts as a base and *vice versa*. At a neutral pH value, reactivity is very low, thus only low ion release should occur. The possible aluminum aqua complexes at the different pH values are shown in Fig. S7.†

The ion release for both Al^0 and Al_2O_3 NMs after one hour was very low, about 0.2–0.4% in BSA and 0.3–0.5% in DMEM (with 10% FCS) (Table 2). As already described above, this was expected at a neutral pH value. For *in vitro* experiments, this will

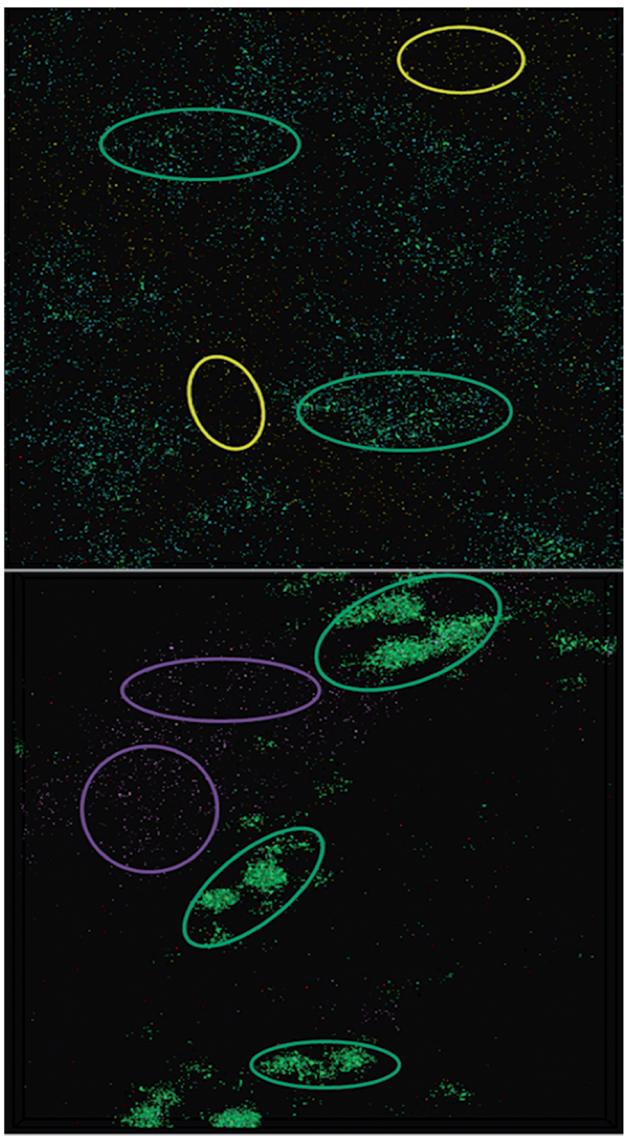

Fig. 9 ToF-SIMS reconstructed ion overlay image (500 μm × 500 μm) of Al NM (top) and Al_2O_3 (bottom) agglomerates of different chemical entities from a DMEM solution; yellow: Al NM, purple: Al_2O_3 NM, green: aluminum(III)–serine; orange: phenylalanine aluminate; red: leucine aluminate; blue: polyoxo-aluminum complex.

Table 3 Main characterization techniques and their limits[a]

Methods		TEM	EELS-TEM	XRD	SAXS	SP-ICP-MS	ICP-MS	ToF-SIMS	IBM, atom number %	CRM
Aluminum	Results	Primary particle size and shape: 2–50 nm, nearly spherical	Core–shell structure, thin (2–5 nm) oxide layer	Aluminum surface; partially oxidized	Particle radius: > 10 nm	Primary particle size: 54–80 nm	Ion release: 0.2–0.5%	Particle-amino acid agglomerates	Impurities: P (1%); biocorona: S (5%), protein; adsorption from DMEM; $Ca_3(PO_4)_2$ coating: P (3%)	No data available
	Limits	No element-specific limits	Light core of Al hinders detailed measurements	No element-specific limits	No element-specific limits	No limits known; results show limit of 54 nm	Detection limit of 10 μg g^{-1} in DMEM	No element-specific limits	From Al to higher atomic mass	Raman active molecules
Al_2O_3	Results	Primary particle size and shape: 10 × 20–50 nm, grain-like shape	Fully oxidized particle	Fully oxidized surface	Primary particle radius: 7.1 nm aggregates' radius: > 10 nm	Primary particle size: 50–80 nm	Ion release: 0.2–0.4%	Particle-amino acid agglomerates; polyoxo-aluminates	Impurities: S (0.2%); biocorona: S (1%), protein adsorption from DMEM; $Ca_3(PO_4)_2$ coating: P (1%)	No data available
	Limits	No element-specific limits	Light core of Al hinders detailed measurements	No element-specific limits	No element-specific limits	No limits known; results show limit of 50 nm	Detection limit of 10 ng g^{-1} in DMEM	No element-specific limits	From Al to higher atomic mass	Raman active molecules
TiO_2 NM103	Results	Primary particle size and shape: 20–100 nm, nearly spherical[b]	No data available	Rutile; crystallite size: 20 nm[b]	Gyration diameter: 26 nm[b]	Primary particle size: 60–100 nm	No solubility in BSA, low soluble in DMEM[b]	Particle-amino acid agglomerates	Impurities: Al (7%), S (0.6%); biocorona: S (0.5%), protein; exchange in DMEM; $Ca_3(PO_4)_2$ coating: P (0.5%)	Decrease of aliphatic/aromatic compounds on NM surface; higher protein exchange in DMEM
	Limits	No element-specific limits	No element-specific limits	No element-specific limits	No element-specific limits	Limit of ∼90 nm[39]	Detection limit of 7.5 ng g^{-1} in DMEM	No element-specific limits	From Al to higher atomic mass	Raman active molecules
TiO_2 NM104	Results	Primary particle size and shape: 10–50 nm, nearly spherical	No data available	Rutile; crystallite size: 21 nm[b]	Gyration diameter: 26 nm[b]	Primary particle size: 60–100 nm	No solubility in BSA, low soluble in DMEM[b]	Particle-amino acid agglomerates	Impurities: Al (6%), S (0.7%); biocorona: S (1%); protein; exchange in DMEM; $Ca_3(PO_4)_2$ coating: P (0.8%)	Decrease of aliphatic/aromatic compounds on NM surface; higher protein exchange in DMEM

Table 3 (*Contd.*)

Methods		TEM	EELS-TEM	XRD	SAXS	SP-ICP-MS	ICP-MS	ToF-SIMS	IBM, atom number %	CRM
	Limits	No element-specific limits	No element-specific limits	No element-specific limits	No element-specific limits	Limit of ~90 nm[39]	Detection limit of 7.5 ng g^{-1} in DMEM	No element-specific limits	From Al to higher atomic mass	Raman active molecules
General limits		1 nm to 2 μm; only dried samples	Organic matrix contaminates sample	Only powder and crystallite samples	r = 0.5–30 nm (depending on the available q-range)	Only highly diluted samples, limits: Au 10 nm, Ag 20 nm	Sub ng g^{-1} level for most elements	No single particles visible, only agglomerates	Only dry samples under vacuum condition, detection limit: few ppm	Only raman active molecules observable

[a] Abbreviations: TEM – transmission electron microscopy; EELS – electron energy loss spectroscopy; XRD – X-ray diffraction; SAXS – small angle X-ray scattering; SP-ICP-MS – single particle inductively coupled plasma mass spectrometry; ICP-MS – inductively coupled plasma mass spectrometry; ToF-SIMS – time of flight mass spectrometry; IBM – Ion beam microscopy; CRM – confocal Raman microscopy; BSA – bovine serum albumin; DMEM – Dulbecco's modified eagle medium; ppm – parts per million. [b] Data taken from (ref. 30).

mean that the effects will originate mainly from particles and not from Al ions. The application of an artificial digestion procedure for mimicking *in vivo* situation showed, that the particle dissolution and complexation behavior was quite different in all three studied gastrointestinal compartments.[24] After no significant changes in the saliva, the gastric environment leads to a significant increase of the dissolution rate as well as very strong agglomeration of NMs. The addition of intestinal fluid results in a nearly neutral pH value which leads to a decrease in the dissolution rate, a deagglomeration of particles and even *de novo* particle formation in ionic aluminum control.

Particle-CCM interactions

It is of major interest to evaluate the elemental and molecular changes on the particle surface during sample preparation for cell experiments (Fig. S8 and S9†). Additionally, two steps were chosen to investigate the surface modification of particles during the sample preparation process. Firstly, the NMs were dispersed. In this step, NMs were covered with albumin corona and are referred to as "BSA" in the text below. The second step was to investigate the NMs under cell culture conditions, diluted in DMEM. After each step, the particles were washed three times in Millipore water. The results of the element analysis, performed by IBM, are shown in Fig. 8.

The variation of the element content represents changes on the surface of NMs, *e.g.* attachment of amino acids, fatty acids, proteins and/or ions to the surface of the NMs. An increase in the Ca and P amount was observed for all studied NMs exposed to DMEM. The highest content of these elements was found in the case of Al NMs. It is suggested that calcium and phosphate ions interact strongly with the albumin corona of NMs and build a calcium phosphate layer on the particle surface. It is known that calcium phosphate has a high affinity to proteins and can increase the efficiency of uptake.[37,38]

The amount of sulfur on the NMs was analyzed under different conditions. Sulfur was found in association with proteins forming a corona around the NMs. Al and Al_2O_3 NMs acquire more proteins on their surface when exposed to DMEM as compared to dispersion in 0.05% BSA (Fig. S11†). In the case of Al and Al_2O_3, the proteins from the culture medium contribute to additional adsorption compared to the existing albumin corona of the particles alone. DMEM shows more physiologic relevant conditions. The salts might induce shielding effects on the protein, so the amount of proteins is likely to be increased. Due to the larger variety of available proteins, a more complex corona will self-assemble on the surface of the particles. In contrast, a decreased amount of proteins was found in the case of NM103 and 104 NMs exposed to DMEM. Substitution of the relatively dense BSA on the particle surface with less dense proteins from the culture media is suggested. This exchange of proteins has a stabilizing effect on TiO_2 NMs in DMEM and results in a strong decrease of aggregate size in DMEM media (Table 1). This finding is also supported by CRM investigations (Fig. S10†).

ToF-SIMS was used to image Al NMs and Al_2O_3 NMs as well as nanoparticle agglomerates in cell culture medium and to assess the chemical composition of the nanoparticle agglomerates. The analyses revealed nanoparticle-specific agglomerates, consisting of polyoxo-aluminum complexes, aluminum(III)–serine and amino acid aluminate complexes (leucine and phenylalanine aluminate). These complexes were not observed when ionic $AlCl_3$ was added to the cell culture medium. ToF-SIMS images revealed a rather homogenous agglomerate distribution with only a slight accumulation of Al NMs in certain areas (see yellow circles in Fig. 9, top) and aluminum(III)–serine and polyoxo-aluminum complexes in others (see green circles in Fig. 9, top). While the aluminates co-locate with both areas, aluminates can be found in regions with predominantly Al NMs and in areas with predominantly aluminum(III)–serine and polyoxo-aluminum. Fig. 9 shows the ToF-SIMS image for Al_2O_3 NMs (bottom). Larger agglomerate areas (green circles in Fig. 9, bottom), where aluminum(III)–serine and polyoxo-aluminum complexes were present in higher amounts, can be distinguished from areas with predominantly smaller nanoparticle agglomerates made of Al_2O_3 NMs (see purple circles in Fig. 9, bottom).

In DMEM with Al NMs, areas where predominantly Al NMs localize, depicted as yellow circles in Fig. 9, top, are distinct from areas where polyoxo-aluminum complexes and aluminum(III)–serine particles localize (green circles). Generally, smaller agglomerates of different chemical entities, Al NMs, aluminum(III)–serine, leucine aluminate, phenylalanine aluminate and polyoxo-aluminum complexes, which do not co-localize in the same area, were observed. In addition to areas where predominantly Al_2O_3 NMs (purple) localize, Al_2O_3 NMs in DMEM show a similar pattern with areas where all chemical entities co-localize but are clearly separated from each other. This indicates a starting mineralization of the larger agglomerates, where different chemical entities co-localize and form mixed agglomerates of Al_2O_3 NMs, amino acids and aluminum salts. Further agglomerate compositions and chemical entities were detected (Fig. S11–14†). For ToF-SIMS measurements for TiO_2 NM103 and 104 in DMEM see Fig. S15–18.†

Conclusions

An extensive characterization of NMs in their different states, from dispersion to *in vitro* conditions, should precede any toxicological testing. In this study, we have characterized two different types of NMs, one metal and one metal oxide. For this purpose, we used a wide range of complementary analytical techniques to characterize particle size, surface and composition in more detail. An in-depth insight into the dissolution, one of the most important determinants of NM toxicity, was achieved by investigation by the examples of Al^0 and Al_2O_3 NMs. A very low dissolution rate and a small percentage of ion release was observed at a neutral pH value, while higher rates for acidic environment we already reported earlier.[24] A significant difference between the surface and the extent of oxidation of Al^0 and Al_2O_3 NM forms was detected. In contrast to the fully oxidized Al_2O_3 with a rather homogenous distribution of Al and O atoms, Al^0 NM showed a core–shell structure with an oxide layer only a few nm thick. This was proven with XRD and the EELS technique, which emphasizes the benefit of using different techniques to get reliable results. It was demonstrated with the help of ToF-SIMS that both aluminum forms are subject to a surprisingly different complexation in biological media: while Al^0 NMs were shown to form complexes with amino acids, Al_2O_3 NMs mostly formed polyoxo-complexes out of two or more Al_2O_3 molecules. Based on the collected results, all of the investigation methods applied have their own benefits. Thus, with the methods described in this study focusing on size, surface and complex formation, dissolution investigations can perhaps become a bit more predictable. Right now, the recommended limit for aluminum release from food is 5 mg kg^{-1} food. The various aluminum forms, *e.g.* ions, micro- and nanomaterials, pure Al^0 or Al_2O_3, are not differentiated here. With this study, it becomes obvious that there should be differentiation for the different forms, as they may be taken up and react differently. For future analytical investigations on aluminum-containing NMs, we propose considering not only Al_2O_3 but also Al^0 NMs and their interaction with the corresponding ions.

Conflicts of interest

There are no conflicts to declare.

Acknowledgements

This French-German bilateral project SolNanoTOX was funded by the German Research Foundation (DFG, Project ID: DFG (FKZ LA 3411/1-1 and LA 1177/9-1)) and the French National Research Agency (ANR, Project ID: ANR-13-IS10-0005). The authors would like to thank Simone Rolf from the Federal Institute for Materials Research and Testing (BAM) for the XRD measurements, Claudia Kästner from BAM for the SAXS measurements and Dr Uwe Mühle from the Fraunhofer Institute for Ceramic Technologies and Systems (IKTS) for the TEM measurements with elemental information.

Notes and references

1 A. Moores and F. Goettmann, *New J. Chem.*, 2006, **30**, 1121–1132.
2 K. L. Kelly, E. Coronado, L. L. Zhao and G. C. Schatz, *J. Phys. Chem. B*, 2003, **107**, 668–677.
3 D. M. Brown, M. R. Wilson, W. MacNee, V. Stone and K. Donaldson, *Toxicol. Appl. Pharmacol.*, 2001, **175**, 191–199.
4 S. Hussain, S. Boland, A. Baeza-Squiban, R. Hamel, L. C. J. Thomassen, J. A. Martens, M. A. Billon-Galland, J. Fleury-Feith, F. Moisan, J. C. Pairon and F. Marano, *Toxicology*, 2009, **260**, 142–149.
5 Y. Zhang, N. Kohler and M. Q. Zhang, *Biomaterials*, 2002, **23**, 1553–1561.
6 A. Cockburn, R. Bradford, N. Buck, A. Constable, G. Edwards, B. Haber, P. Hepburn, J. Howlett, F. Kampers, C. Klein, M. Radomski, H. Stamm, S. Wijnhoven and T. Wildemann, *Food Chem. Toxicol.*, 2012, **50**, 2224–2242.
7 I. A. Rahman, P. Vejayakumaran, C. S. Sipaut, J. Ismail and C. K. Chee, *Mater. Chem. Phys.*, 2009, **114**, 328–332.

8 S. E. A. Gratton, P. A. Ropp, P. D. Pohlhaus, J. C. Luft, V. J. Madden, M. E. Napier and J. M. DeSimone, *Proc. Natl. Acad. Sci. U. S. A.*, 2008, **105**, 11613–11618.
9 Y. Zhou and M. Antonietti, *J. Am. Chem. Soc.*, 2003, **125**, 14960–14961.
10 S. K. Das, M. K. Bhunia and A. Bhaumik, *Dalton Trans.*, 2010, **39**, 4382–4390.
11 Z. Q. Sun, T. Liao, L. Y. Sheng, L. Z. Kou, J. H. Kim and S. X. Dou, *Chem.–Eur. J.*, 2016, **22**, 11357–11364.
12 X. N. Ren, L. Wu, J. Jin, J. Liu, Z. Y. Hu, Y. Li, T. Hasan, X. Y. Yang, G. Van Tendeloo and B. L. Su, *RSC Adv.*, 2016, **6**, 26856–26862.
13 M. Moreno-Horn and T. Gebel, *Crit. Rev. Toxicol.*, 2014, **44**, 849–875.
14 J. X. Wang, G. Q. Zhou, C. Y. Chen, H. W. Yu, T. C. Wang, Y. M. Ma, G. Jia, Y. X. Gao, B. Li, J. Sun, Y. F. Li, F. Jiao, Y. L. Zhao and Z. F. Chai, *Toxicol. Lett.*, 2007, **168**, 176–185.
15 E. J. Park, H. Kim, Y. Kim and K. Choi, *Toxicol. Environ. Chem.*, 2011, **93**, 120–133.
16 Y. R. Kim, S. Y. Lee, E. J. Lee, S. H. Park, N. W. Seong, H. S. Seo, S. S. Shin, S. J. Kim, E. H. Meang, M. K. Park, M. S. Kim, C. S. Kim, S. K. Kim, S. W. Son, Y. R. Seo, B. H. Kang, B. S. Han, S. S. Aan, B. J. Lee and M. K. Kim, *Int. J. Nanomed.*, 2014, **9**, 67–78.
17 K. Loeschner, N. Hadrup, K. Qvortrup, A. Larsen, X. Y. Gao, U. Vogel, A. Mortensen, H. R. Lam and E. H. Larsen, *Part. Fibre Toxicol.*, 2011, **8**, 18.
18 J. H. E. Arts, M. Hadi, A. M. Keene, R. Kreiling, D. Lyon, M. Maier, K. Michel, T. Petry, U. G. Sauer, D. Warheit, K. Wiench and R. Landsiedel, *Regul. Toxicol. Pharmacol.*, 2014, **70**, 492–506.
19 A. R. Collins, B. Annangi, L. Rubio, R. Marcos, M. Dorn, C. Merker, I. Estrela-Lopis, M. R. Cimpan, M. Ibrahim, E. Cimpan, M. Ostermann, A. Sauter, N. E. Yamani, S. Shaposhnikov, S. Chevillard, V. Paget, R. Grall, J. Delic, F. G. de-Cerio, B. Suarez-Merino, V. Fessard, K. N. Hogeveen, L. M. Fjellsbo, E. R. Pran, T. Brzicova, J. Topinka, M. J. Silva, P. E. Leite, A. R. Ribeiro, J. M. Granjeiro, R. Grafstrom, A. Prina-Mello and M. Dusinska, *Wiley Interdiscip. Rev.: Nanomed. Nanobiotechnol.*, 2017, **9**, e1413.
20 P. Laux, C. Riebeling, A. M. Booth, J. D. Brain, J. Brunner, C. Cerrillo, O. Creutzenberg, I. Estrela-Lopis, T. Gebel, G. Johanson, H. Jungnickel, H. Kock, J. Tentschert, A. Tlili, A. Schäffer, A. J. A. M. Sips, R. A. Yokel and A. Luch, *NanoImpact*, 2017, **6**, 69–80.
21 J. M. Cohen, J. G. Teeguarden and P. Demokritou, *Part. Fibre Toxicol.*, 2014, **11**, 20.
22 S. Dekkers, A. G. Oomen, E. A. J. Bleeker, R. J. Vandebriel, C. Micheletti, J. Cabellos, G. Janer, N. Fuentes, S. Vazquez-Campos, T. Borges, M. J. Silva, A. Prina-Mello, D. Movia, F. Nesslany, A. R. Ribeiro, P. E. Leite, M. Groenewold, F. R. Cassee, A. J. A. M. Sips, A. Dijkzeul, T. van Teunenbroek and S. W. P. Wijnhoven, *Regul. Toxicol. Pharmacol.*, 2016, **80**, 46–59.
23 A. D. Maynard, R. J. Aitken, T. Butz, V. Colvin, K. Donaldson, G. Oberdorster, M. A. Philbert, J. Ryan, A. Seaton, V. Stone, S. S. Tinkle, L. Tran, N. J. Walker and D. B. Warheit, *Nature*, 2006, **444**, 267–269.
24 H. Sieg, C. Kastner, B. Krause, T. Meyer, A. Burel, L. Bohmert, D. Lichtenstein, H. Jungnickel, J. Tentschert, P. Laux, A. Braeuning, I. Estrela-Lopis, F. Gauffre, V. Fessard, J. Meijer, A. Luch, A. F. Thunemann and A. Lampen, *Langmuir*, 2017, **33**, 10726–10735.
25 J. M. Zook, S. E. Long, D. Cleveland, C. L. A. Geronimo and R. I. MacCuspie, *Anal. Bioanal. Chem.*, 2011, **401**, 1993–2002.
26 K. Loza, J. Diendorf, C. Sengstock, L. Ruiz-Gonzalez, J. M. Gonzalez-Calbet, M. Vallet-Regi, M. Koller and M. Epple, *J. Mater. Chem. B*, 2014, **2**, 1634–1643.
27 Z. Y. Wang, A. von dem Bussche, P. K. Kabadi, A. B. Kane and R. H. Hurt, *ACS Nano*, 2013, **7**, 8715–8727.
28 A. M. Tavares, H. Louro, S. Antunes, S. Quarre, S. Simar, P. J. De Temmerman, E. Verleysen, J. Mast, K. A. Jensen, H. Norppa, F. Nesslany and M. J. Silva, *Toxicol. in Vitro*, 2014, **28**, 60–69.
29 H. E. Pace, N. J. Rogers, C. Jarolimek, V. A. Coleman, C. P. Higgins and J. F. Ranville, *Anal. Chem.*, 2011, **83**, 9361–9369.
30 K. Rasmussen, J. Mast, P. J. de Temmerman, E. Verleysen, N. Wegeneers, F. van Steen, J. C. Pizzolon, L. de Temmerman, E. van Doren, K. A. Jensen, R. Birkedal, M. Levin, S. H. Nielsen, I. K. Koponen, P. A. Clausen, V. Kofored-Sørensen, Y. Kembouche, N. Thieriet, O. Spalla, C. Giuot, D. Rousset, O. Witschger, S. Bau, B. Bianchi, C. Motzkus, B. Shivachev, L. Dimowa, R. Nikolova, D. Nihtianova, M. Tarassov, O. Petrov, S. Bakardjieva, D. Gilliland, F. Pianella, G. Ceccone, V. Spampinato, G. Cotogno, P. Gibson, C. Gaillard and A. Mech, JRC Science and Policy Reports, 2014, http://publications.jrc.ec.europa.eu/repository/handle/JRC86291.
31 M. Naiim, A. Boualem, C. Ferre, M. Jabloun, A. Jalocha and P. Ravier, *Soft Matter*, 2015, **11**, 28–32.
32 P. A. Hassan and S. K. Kulshreshtha, *J. Colloid Interface Sci.*, 2006, **300**, 744–748.
33 R. D. Deegan, O. Bakajin, T. F. Dupont, G. Huber, S. R. Nagel and T. A. Witten, *Nature*, 1997, **389**, 827–829.
34 P. J. De Temmerman, E. Van Doren, E. Verleysen, Y. Van der Stede, M. A. D. Francisco and J. Mast, *J. Nanobiotechnol.*, 2012, **10**, 24.
35 P. Muneesawang and C. Sirisathitkul, *J. Nanomater.*, 2015, **2015**, 8.
36 R. J. Griffitt, A. Feswick, R. Weil, K. Hyndman, P. Carpinone, K. Powers, N. D. Denslow and D. S. Barber, *Environ. Toxicol.*, 2011, **26**, 541–551.
37 T. T. Morgan, H. S. Muddana, E. I. Altinoglu, S. M. Rouse, A. Tabakovic, T. Tabouillot, T. J. Russin, S. S. Shanmugavelandy, P. J. Butler, P. C. Eklund, J. K. Yun, M. Kester and J. H. Adair, *Nano Lett.*, 2008, **8**, 4108–4115.
38 G. Dordelmann, D. Kozlova, S. Karczewski, R. Lizio, S. Knauer and M. Epple, *J. Mater. Chem. B*, 2014, **2**, 7250–7259.
39 S. Lee, X. Y. Bi, R. B. Reed, J. F. Ranville, P. Herckes and P. Westerhoff, *Environ. Sci. Technol.*, 2014, **48**, 10291–10300.

Characterization of aluminum, aluminum oxide and titanium dioxide nanomaterials using a combination of methods for particle surface and size analysis

B. Krause*[a], T. Meyer[b], H. Sieg[c], C. Kästner[d], P. Reichardt[a], J. Tentschert[a], H. Jungnickel[a], I. Estrela-Lopis[b], A. Burel[e], S. Chevance[f], F. Gauffre[f], P. Jalili[g], J. Meijer[h], L. Boehmert[c], A. Braeuning[c], A. F. Thünemann[d], F. Emmerling,[i] V. Fessard[g], P. Laux[a], A. Lampen[c] and A. Luch[a]

[a] German Federal Institute for Risk Assessment (BfR), Department of Chemical and Product Safety, Max-Dohrn-Straße 8-10, 10589 Berlin, Germany
[b] Institute of Medical Physics and Biophysics, University of Leipzig, Härtelstrasse 16-18, 04275 Leipzig, Germany
[c] German Federal Institute for Risk Assessment (BfR), Department of Food Safety, Max-Dohrn-Straße 8-10, 10589 Berlin, Germany
[d] Federal Institute for Materials Research and Testing (BAM), Unter den Eichen 87, 12205 Berlin, Germany
[e] MRIC TEM BIOSIT, Université de Rennes 1, 2 av pro Leon Bernard, France
[f] Institut des Sciences Chimiques de Rennes, UMR-CNRS 6226, Université de Rennes 1, France
[g] ANSES, French Agency for Food, Environmental and Occupational Health Safety, Fougères Laboratory, 10B rue Claude Bourgelat, 35306, Fougères Cedex, France

Supporting Information

Figure S1: NTA averaged distributions

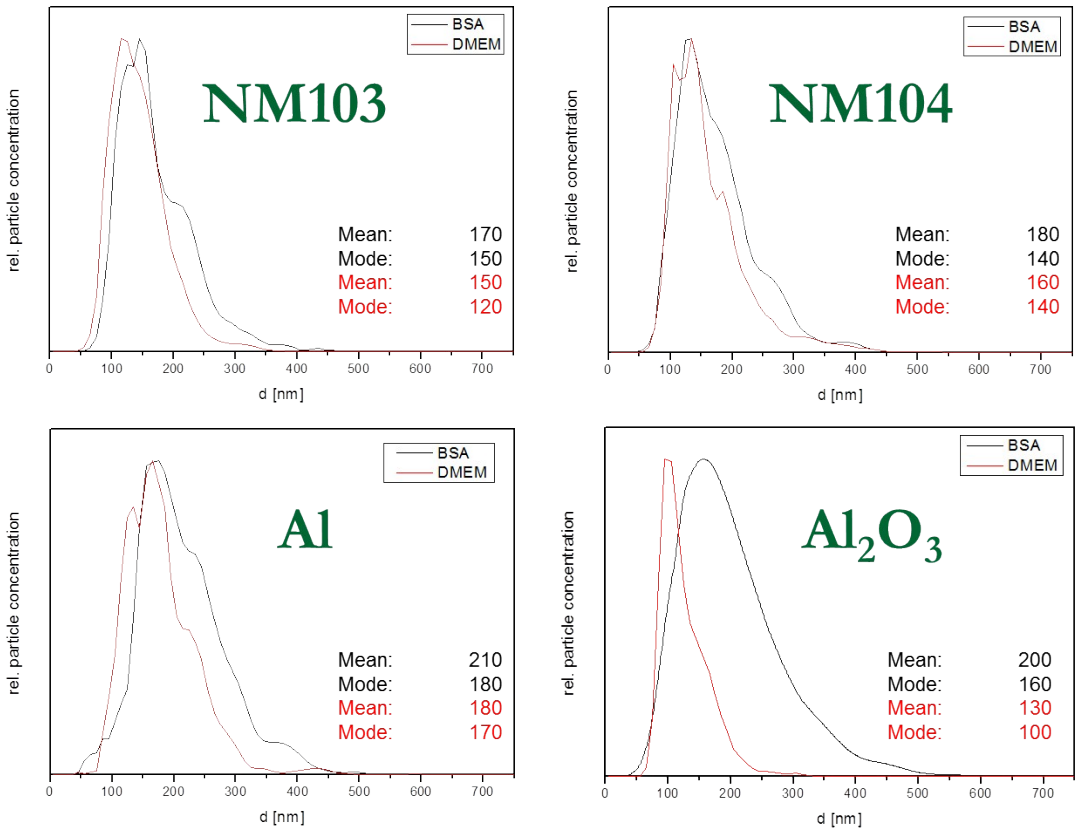

Figure S1: Averaged size distributions of NM103, NM104, Al and Al_2O_3 recorded by NTA. Y-axis: Relative particle concentration; x-axis: hydrodynamic diameter. Black: NMs prepared after Nanogenotox protocol; red: size distribution of NMs under cell culture conditions. BSA: bovine serum albumin; DMEM: Dulbecco's modified eagle medium.

Table S1: Number size distributions by calculation from DLS data

Table S1 Number size distribution with standard deviation (SD) of Al^0, Al_2O_3, NM103 and NM104 NMs in different media calculated based on the intensity size distribution data determined by dynamic light scattering (DLS). All results represent the average of six repeats. BSA: bovine serum albumin; DMEM: Dulbecco's modified eagle medium; FCS: fetal calf serum

	DLS measurements and comparison	
	Lab 1 (Malvern)	Lab 2 (Brookhaven)
	Number-based size [nm]	Number-based size [nm]
	Stock solution (0.05 % BSA in H_2O)	
Al^0 NM	240 ± 10	120 ± 30
Al_2O_3 NM	110 ± 10	80 ± 40
NM103	140 ± 10	250 ± 90
NM104	100 ± 10	200 ± 50
	DMEM (with 10 % FCS)	
Al^0 NM	160 ± 10	80 ± 10
Al_2O_3 NM	10 ± 1	110 ± 70
NM103	110 ± 10	90 ± 10
NM104	110 ± 10	110 ± 10

The size and size distribution of NMs in number-based DLS measurement mode is interesting for a better comparison with other number-based techniques. To compare DLS data to number-based NTA data, a calculation based on the refractive index and the absorption of the used NMs is possible. While both size distributions are correct, some assumptions need to be taken into account:

a. The involvement of the Mie scattering for the more complicated scattering process for particles much smaller than the wavelength of illuminating light (633 nm for Zetasizer ZS, 640 nm for ZetaPALS)
b. Known optical properties of the investigated NMs
c. good raw data quality (broader distributions or high polydispersity can significantly influence the transition from intensity-based to number based distributions)

In our case, we decided to use the intensity-based distribution only, as there are no assumptions needed compared to the transformation into number-based distributions.

Figure S2: TEM measurement of TiO_2 NMs in DMEM

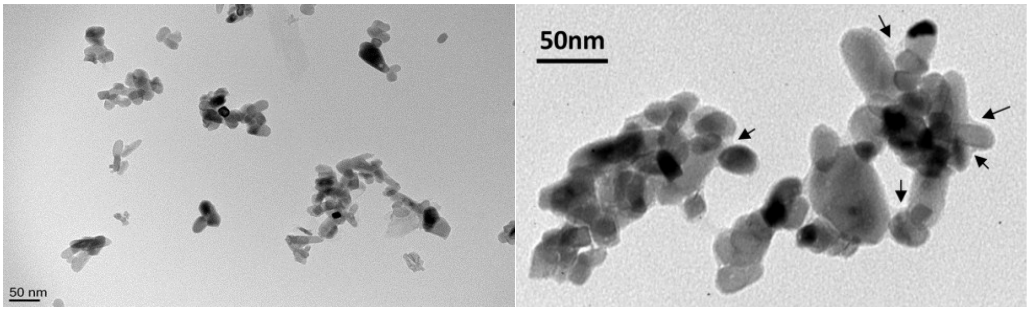

Figure S2: TEM observation of TiO_2 NMs in BSA (left) and DMEM (right) achieved at 80 kV (0.8 g L^{-1}). Arrows show protein deposition.

Figure S3 – S5: SAXS curves fitted with Monte Carlo based data evaluation

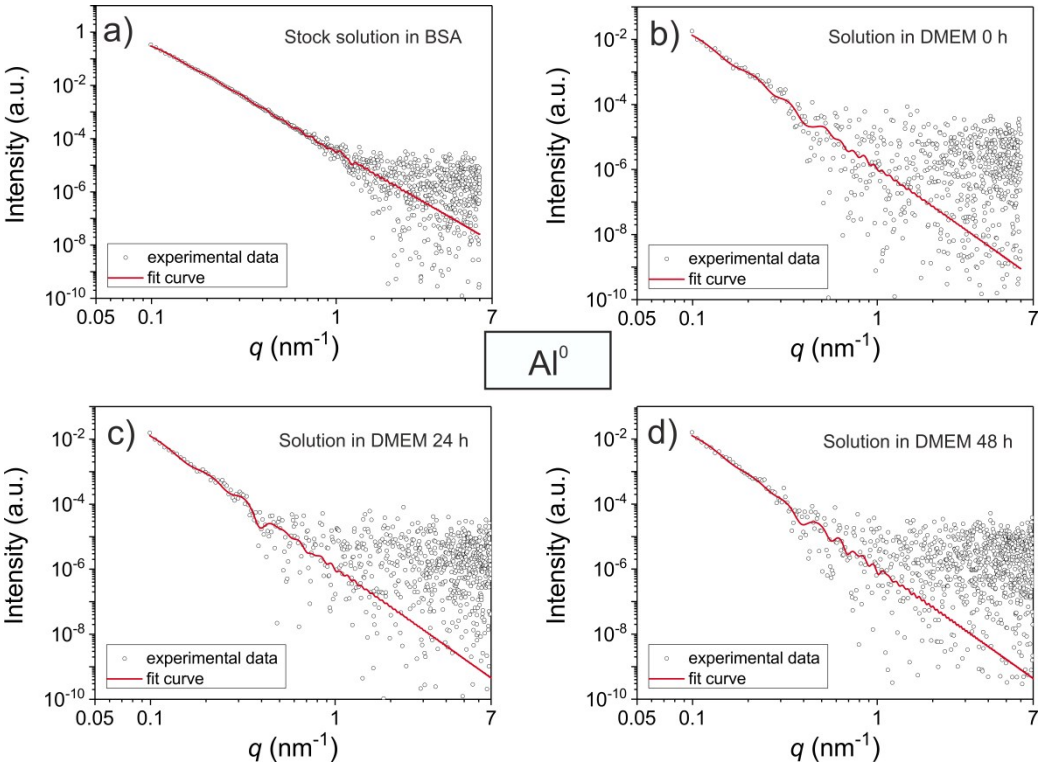

Figure S3: Measured SAXS curves (black circles) of Al NM in (a) stock solution (BSA), (b) directly after addition in DMEM, (c) after 24 h in DMEM and (d) after 48 h in DMEM. The measured data are fitted with a Monte Carlo based data evaluation (red solid lines).

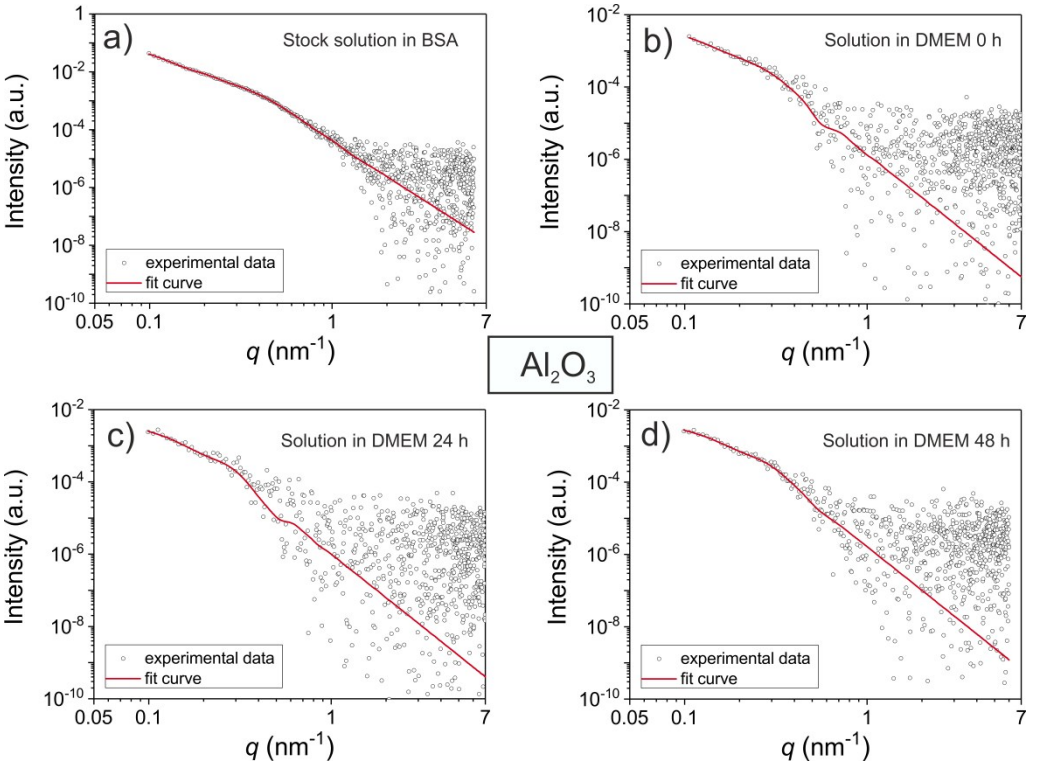

Figure S4: Measured SAXS curves (black circles) of Al_2O_3 NM in (a) stock solution (BSA), (b) directly after addition in DMEM, (c) after 24 h in DMEM and (d) after 48 h in DMEM. The measured data are fitted with a Monte Carlo based data evaluation (red solid lines).

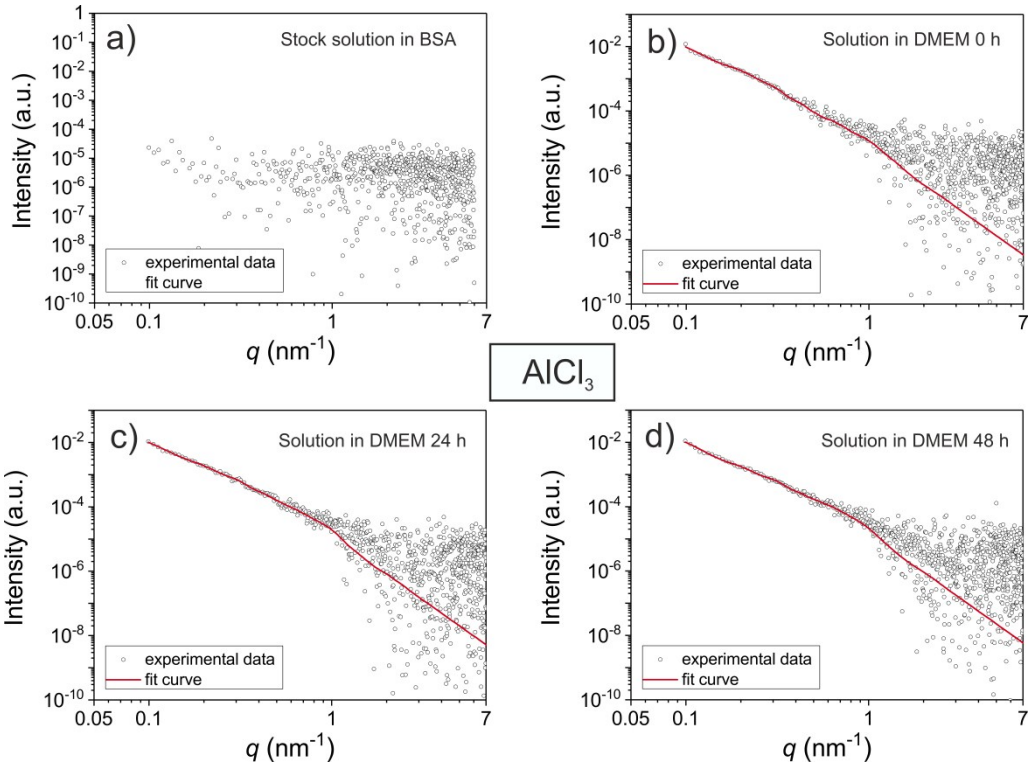

Figure S5: Measured SAXS curves (black circles) of $AlCl_3$ in (a) aqueous stock solution (b) directly after addition in DMEM, (c) after 24 h in DMEM and (d) after 48 h in DMEM. The measured data are fitted with a Monte Carlo based data evaluation (red solid lines).

Figure S6: Impurities of used NMs determined by IBM

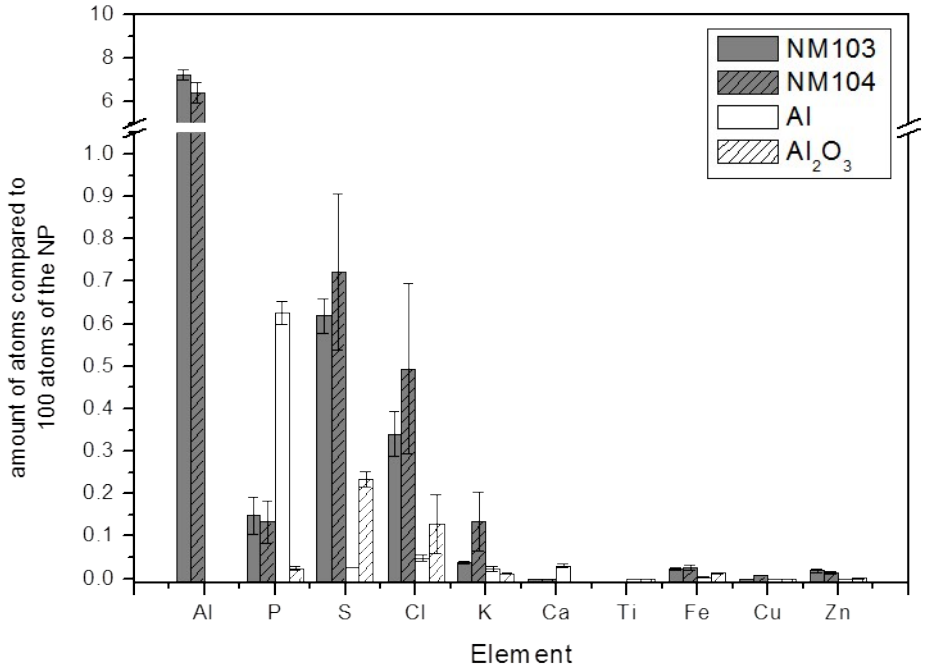

Figure S6: Impurities associated to the NMs as purchased. The impurities are given in number of atoms compared to one hundred atoms of the NMs. In case of TiO_2 titanium isn't shown as well as in case of aluminum containing materials aluminum isn't displayed in the graph.

Figure S7: Aluminum aqua complexes at different pH values

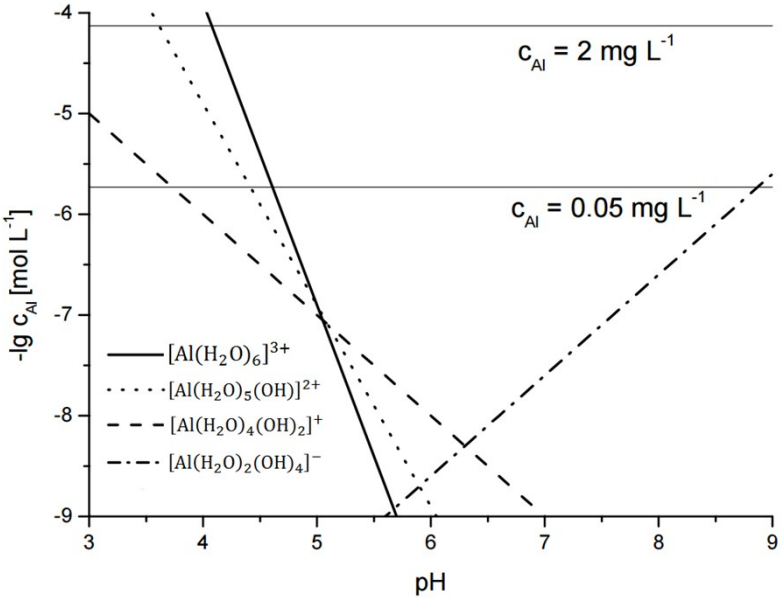

Figure S7: Solubility of Al^{3+} function of pH in equilibrium with $Al(OH)_{3(s)}$, solubility product of $Al(OH)_3$ $KS=10^{-33.9}$ (modified according to Sigg & Stumm 1989) [1].

Figure S8: CRM surface investigations

CRM was applied to study the organic constituents on the surface of the NMs. Figure S8 shows the average Raman spectra of TiO_2 NMs extracted from their spectral images based on the intensity distribution of E_g band of rutile phase, 450 cm^{-1} [2]. The spectra were weighted to integral intensity of NM phonon bands.

For both particles, four main peaks are observable. The peak around 1000 cm^{-1} is a double peak consisting of 988 cm^{-1} induced by ring stretching and 1006 cm^{-1} attributed to ring deformation. These peaks indicate the presence of an aromatic ring structure associated with the particle surface. The region from 1500 to 1700 represents an overlap of different possible structures, e.g. cyclic compounds, double bounds and amide bands [3]. The high variety of possible structures makes clear assignments complicated [3]. The CH_2/CH_3 vibration modes were detected in the region from 2850 to 3000 cm^{-1} attributed to symmetrical and asymmetric CH_2 and CH_3 stretching vibrations and at 1450 cm^{-1} related to $\delta(CH_2)$ and asymmetric $\delta(CH_3)$ deformations [3]. These bands can be associated with aliphatic compounds. The Raman spectra of the hydrophobic NM103 revealed a higher concentration of organic surfactants and aromatic compounds on their surface compared to NM104 NMs.

Both NMs exhibit decreased signals of aromatic and aliphatic compounds on their surface after the treatment with ultra-sonic compared to particles without ultra-sonication. This reveals a loss of organic compounds during the ultra-sonication step.

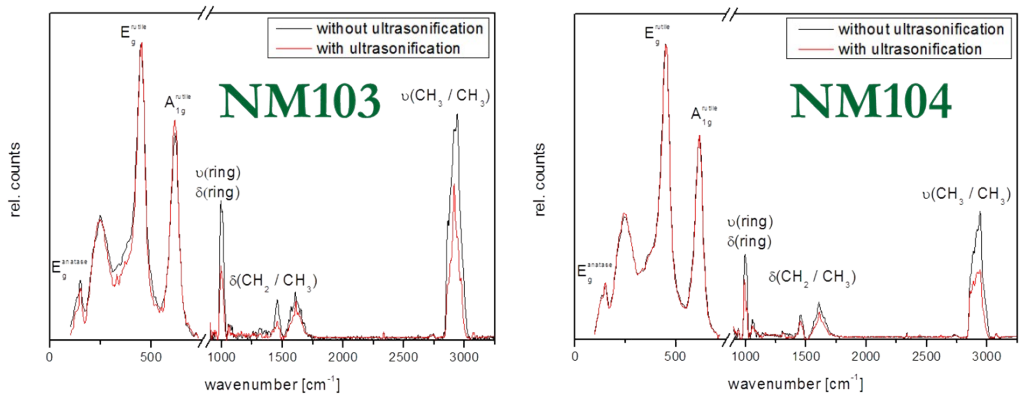

Figure S8: Raman spectra of NMs without and with ultra-sonic treatment. For better visualization, the regions between 900 and 3250 cm^{-1} in both graphs were multiplied by a scaling factor of ten.

Figure S9: Colocalization pattern by IBM

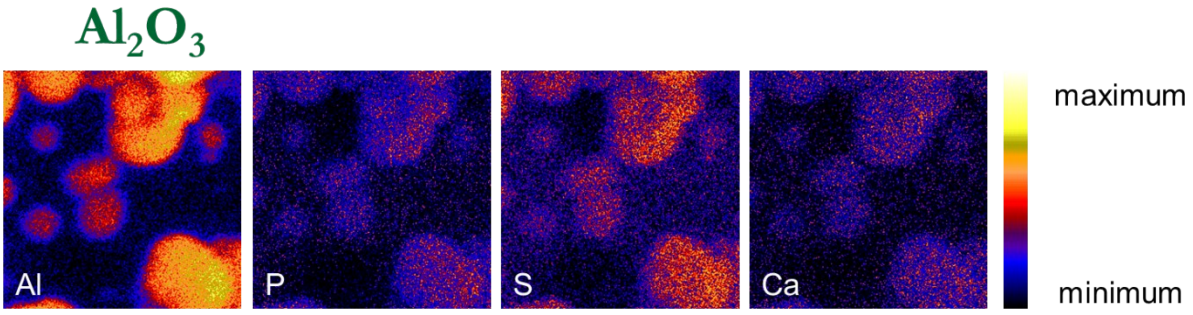

Figure S9: IBM element maps of Al_2O_3 and as purchased only diluted in mpH_2O. The images exhibiting colocalization pattern of the different elements. An area of 50 x 50 µm² is displayed. The color code is as follows: white represents highest concentration and black the lowest concentration.

Figure S10: Influence of different proteins detected by CRM

The bands associated with CH_2/CH_3 vibration modes exhibit the same extent of intensity decrease for both TiO_2 NMs comparing BSA and DMEM conditions as observed by element analysis (Figure S10). Furthermore, the analysis of phonon bands revealed that the crystal structure of both TiO_2 NMs was not affected during the particle preparation process.

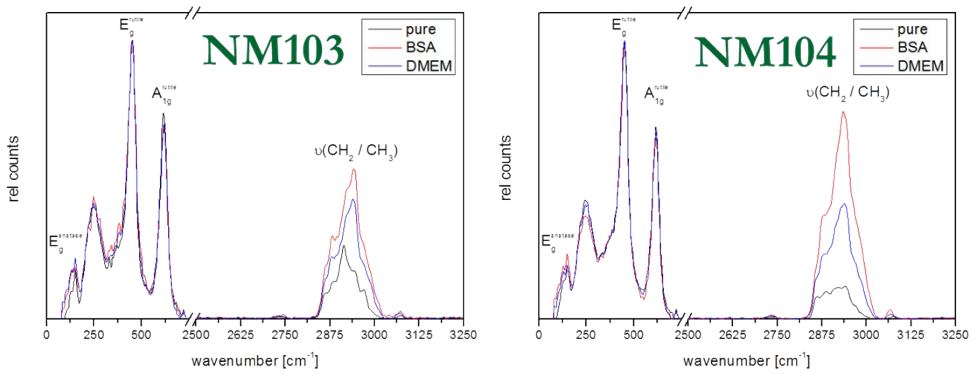

Figure S10: CRM spectra represent the modifications during the preparation process for NM103 (left) and NM104 (right). Pure: particles as purchased; BSA: albumin-coated particles (NanoGenoTOX protocol); DMEM: albumin-coated particles dispersed in DMEM. For better visualization, the regions between 2500 and 3250 cm^{-1} in both graphs were multiplied by a scaling factor of five.

Figure S11 – 14: ToF-SIMS measurements of Al and Al_2O_3 NMs in DMEM

In stock dispersion the albumin concentration is 0.5mg/ml. In DMEM containing FBS the albumin content is about 2mg/ml and about 2.7-4mg/ml other not more specified proteins are included. In addition, the dilution into DMEM was done out of stock dispersion, which already contains 0.5 mg/ml albumin. Using a dilution factor of about 25, 0.02 mg/ml from the BSA stock dispersion, as well as 2 mg/ml albumin and 2.7-4 mg/ml other proteins results in an about 10-times higher protein concentration of DMEM compared to BSA.

Figure S11 shows the distribution of all nanoparticle agglomerates for aluminum nanoparticles and all the different chemical entities (polyoxo-aluminum complex, aluminum-(III)-serine, leucine aluminate and phenylalanine aluminate) separated for each chemical species. All chemical species are clearly separated from each other and located in different areas of the image as specific single agglomerates, which do not co-locate with each other. Figure S12 shows the magnified area, where predominantly Al_2O_3 NMs (shown in purple) agglomerates are located. In these areas of the DMEM with Al_2O_3 NMs single agglomerates, which do not co-localize, made of different chemical entities can be found. Figure S13 shows a magnified area, where larger agglomerates can be found, which largely consist of polyoxo-aluminum complexes and aluminum-(III)-serine. Figure S14 shows a magnification of one of the agglomerate areas. Here regions can be spotted, where polyoxo-aluminum complexes (depicted in blue) and aluminum-(III)-serine (depicted in green) co-localize (see red circles) and areas, where phenylalanine aluminate (depicted in orange) and aluminum-(III)-serine (depicted in green) co-localize (orange circles) as well as areas, where Al_2O_3 NMs (depicted in purple) and aluminum-(III)-serine (depicted in green) co-localize in the same location. These areas may be agglomerates, where a beginning mineralization combines different chemical entities in larger agglomerates.

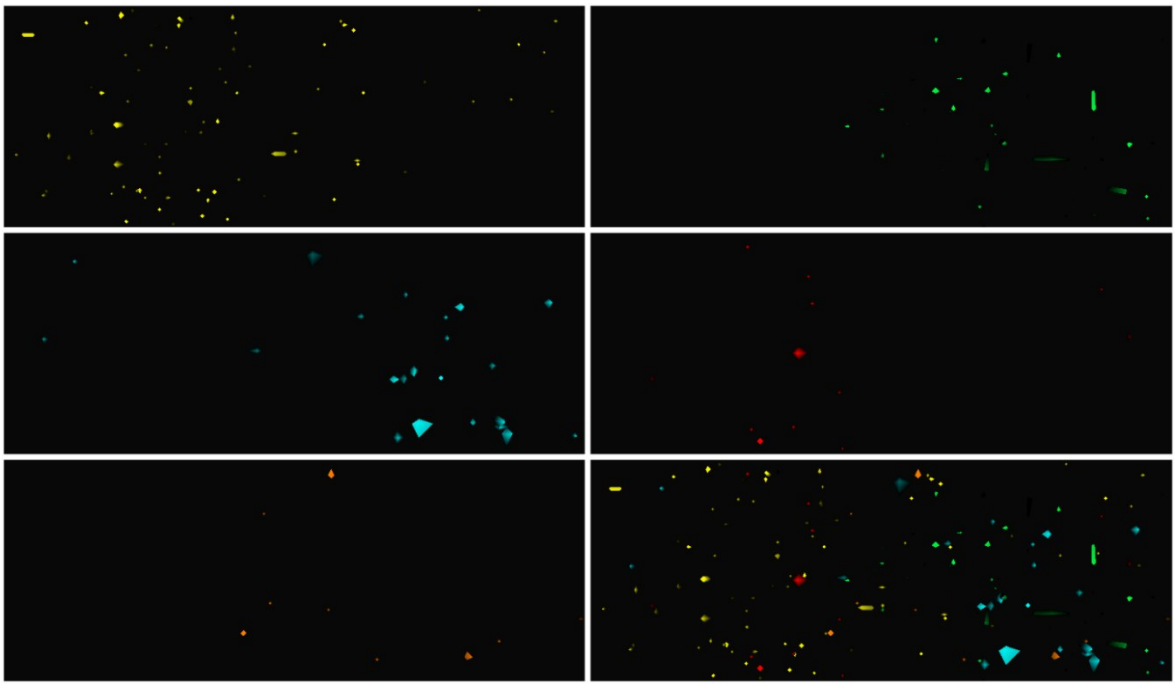

Figure S11: ToF-SIMS reconstructed ion images (90 µm x 30 µm) of Al NMs agglomerates of different chemical entities from DMEM; yellow: Al NMs (a), green: aluminum-(III)-serine (b); orange: phenylalanine aluminate (e); red: leucine aluminate (d); blue: polyoxo-aluminum complex (c). (f) shows an overlay of all ions. In the overlay picture, all chemical entities are separated from each other and do not co-localize.

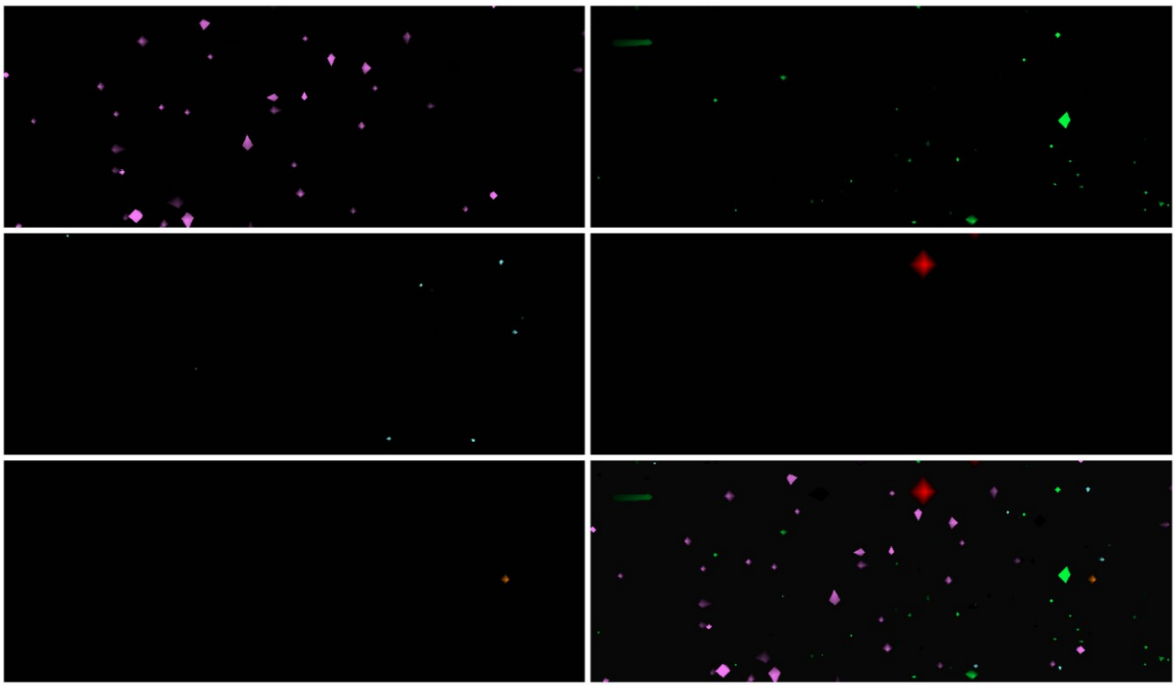

Figure S12: ToF-SIMS reconstructed ion images (90 µm x 30 µm) of Al_2O_3 NMs agglomerates of different chemical entities from DMEM; purple: Al_2O_3 NMs (a), green: aluminum-(III)-serine (b); orange: phenylalanine aluminate (e); red: leucine aluminate (d); blue: polyoxo-aluminum complex (c). (f) shows an overlay of all ions. In the overlay picture, all chemical entities are separated from each other and do not co-localize.

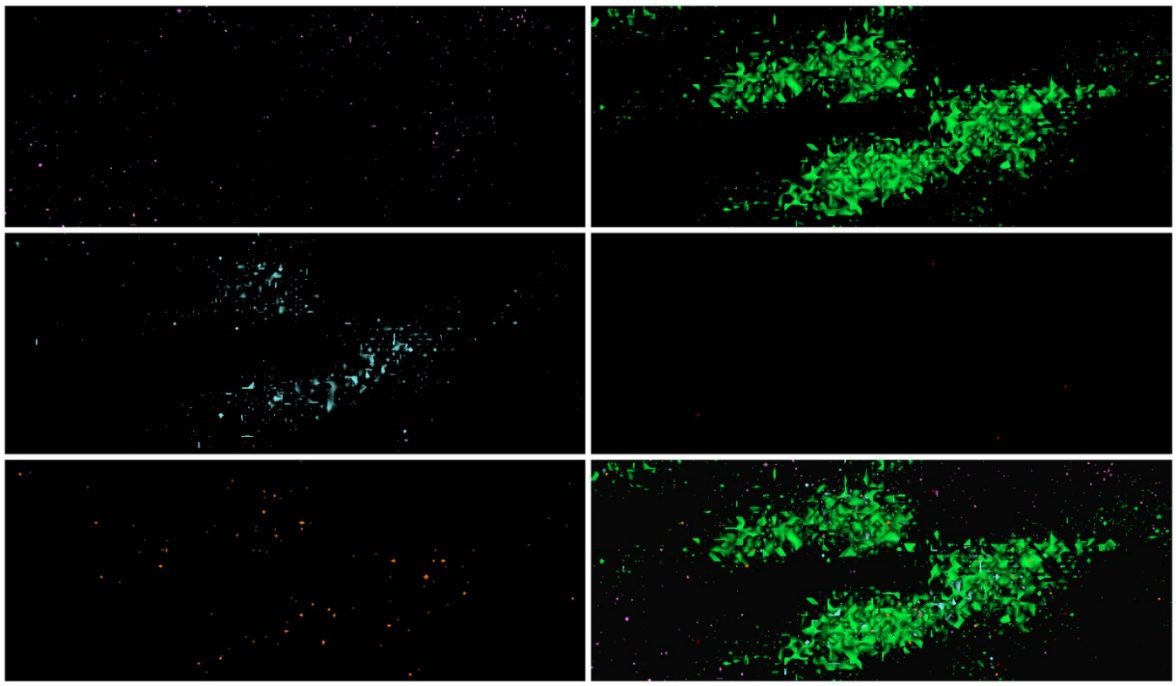

Figure S13: ToF-SIMS reconstructed ion images (90 µm x 30 µm) of Al_2O_3 NMs agglomerates of different chemical entities from DMEM; purple: Al_2O_3 NMs (a), green: aluminum-(III)-serine (b); orange: phenylalanine aluminate (e); red: leucine aluminate (d); blue: polyoxo-aluminum complex (c). (f) shows an overlay of all ions. In the overlay picture, specific areas are visible, where predominantly polyoxo-aluminum complex and aluminum-(III)-serine co-localize in larger agglomerate areas.

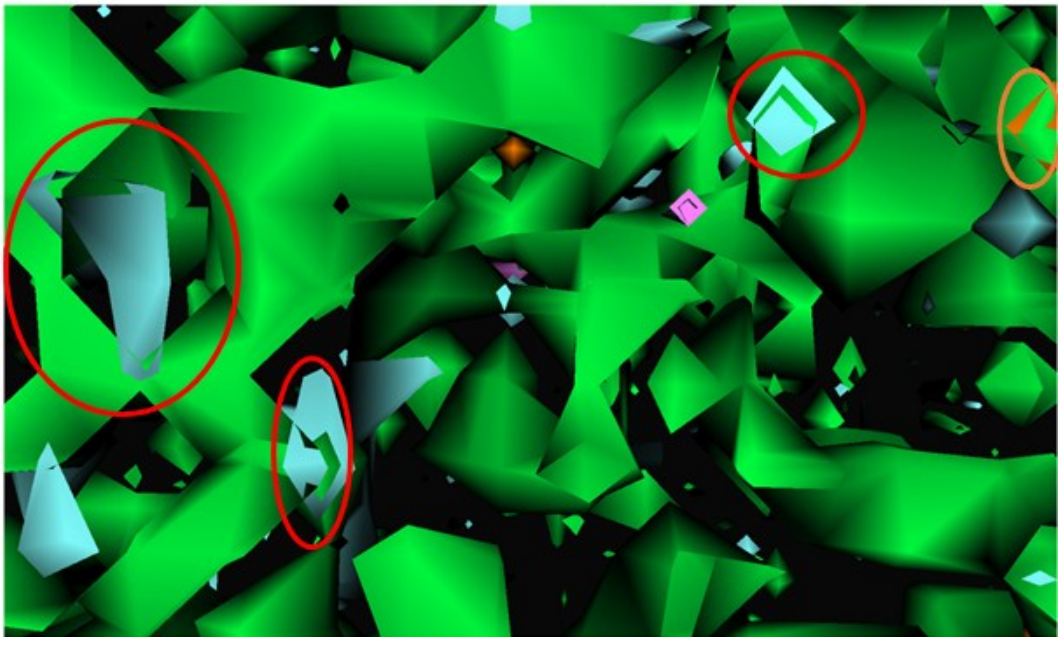

Figure S14: ToF-SIMS reconstructed ion images (20 µm x 10 µm) of Al_2O_3 NMs agglomerates of different chemical entities from DMEM; purple: Al_2O_3 NMs, green: aluminum-(III)-serine; orange: phenylalanine aluminate; red: leucine aluminate; blue: polyoxo-aluminum complex. The picture shows an overlay of all ions. Here specific areas are visible, where polyoxo-aluminum complex (blue) and aluminum-(III)-serine (green) co-localize (see red circles) and areas, where phenylalanine aluminate (orange) and aluminum-(III)-serine (green) co-localize (orange circles) as well as areas, where Al_2O_3 NMs (purple) and aluminum-(III)-serine (green) co-localize in the same location.

Figure S15 – 18: ToF-SIMS measurements of TiO_2 NMs in DMEM

ToF-SIMS was used to visualize TiO_2 NM103 and TiO_2 NM104 as well as nanoparticle agglomerates in DMEM to assess the chemical composition of the nanoparticle agglomerates. The analyses revealed nanoparticle-specific agglomerates, consisting of $TiOH^+$ amino acid complexes TiO_2 amino acid complexes were identified previously as one possible absorption mechanism and it was shown that there was selective absorption of serine on TiO_2 surfaces in benthic microbial fuel cells [4]. Also, adsorption of phenylalanine could already be observed on TiO_2 nanoparticles [5].

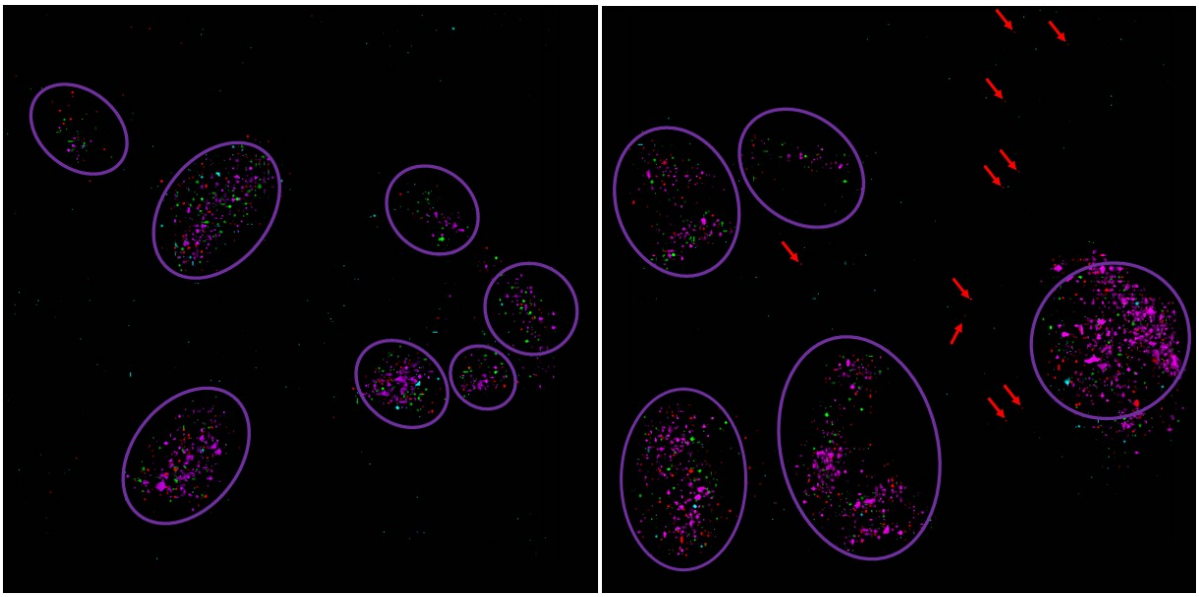

Figure S15: Left: ToF-SIMS reconstructed ion overlay image (500 µm x 500 µm) of TiO_2 NM 103 (left) and NM104 (right) agglomerates of different chemical entities from a DMEM solution; green: TiO_2 NM, blue: $TiOH^+$-serine; purple: $TiOH^+$ -leucine; red: $TiOH^+$ -phenylalanine complex. Purple circles show areas where agglomerates accumulate. Red arrows show single $TiOH^+$-phenylalanine aggregates outside of purple circle areas.

Figure S15 shows the ToF-SIMS image for TiO_2 NM103 (left) and TiO_2 NM104 (right). Larger agglomerate areas (purple circles in Figure S15, left and right), where $TiOH^+$-leucine complexes are present in higher amounts, can be distinguished from areas with predominantly smaller NM agglomerates, made predominantly of $TiOH^+$-serine in Figure S15 (left) showing TiO_2 NM103 while in Figure S15 (right), in addition to $TiOH^+$-serine, $TiOH^+$-phenylalanine aggregates can also be found (see red arrows in Figure S15 (right) and Figure S18). For further information about the distribution of all NM agglomerates for TiO_2 NM103 and TiO_2 NM104 and all the different chemical entities ($TiOH^+$-serine, $TiOH^+$-leucine, $TiOH^+$-phenylalanine) separated for each chemical species, see Figures S14 and S15. All chemical species are clearly separated from each other and located in different areas of the image as specific single agglomerates, which do not co-locate with each other.

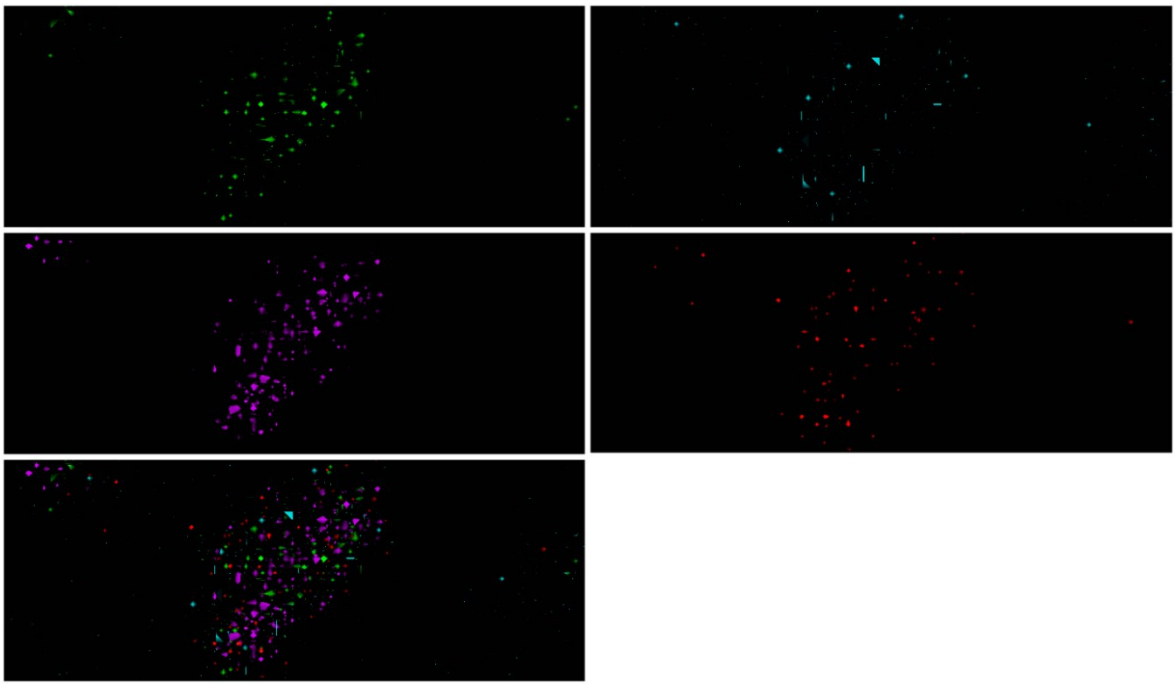

Figure S16: ToF-SIMS reconstructed ion images (90 µm x 30 µm) of TiO_2 NM-103 NMs agglomerates of different chemical entities from DMEM; green: TiO_2 NM (NM-103) (a), blue: $TiOH^+$-serine (b); purple: $TiOH^+$ -leucine (c); red: $TiOH^+$ -phenylalanine (d); (e) shows an overlay of all ions. In the overlay picture, all chemical entities are separated from each other and do not co-localize.

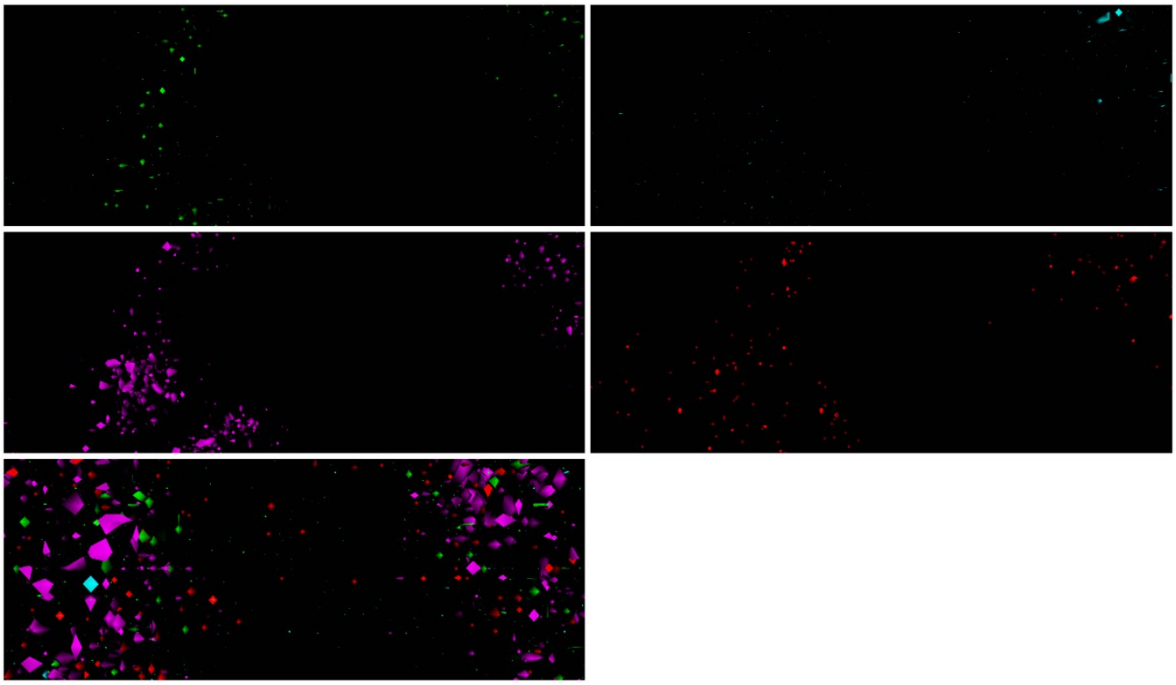

Figure S17: ToF-SIMS reconstructed ion images (90 µm x 30 µm) of TiO_2 NM-104 NMs agglomerates of different chemical entities from DMEM; green: TiO_2 NM (NM-104) (a), blue: $TiOH^+$-serine (b); purple: $TiOH^+$ -leucine (c); red: $TiOH^+$ -phenylalanine (d); (e) shows an overlay of all ions. In the overlay picture, all chemical entities are separated from each other and do not co-localize.

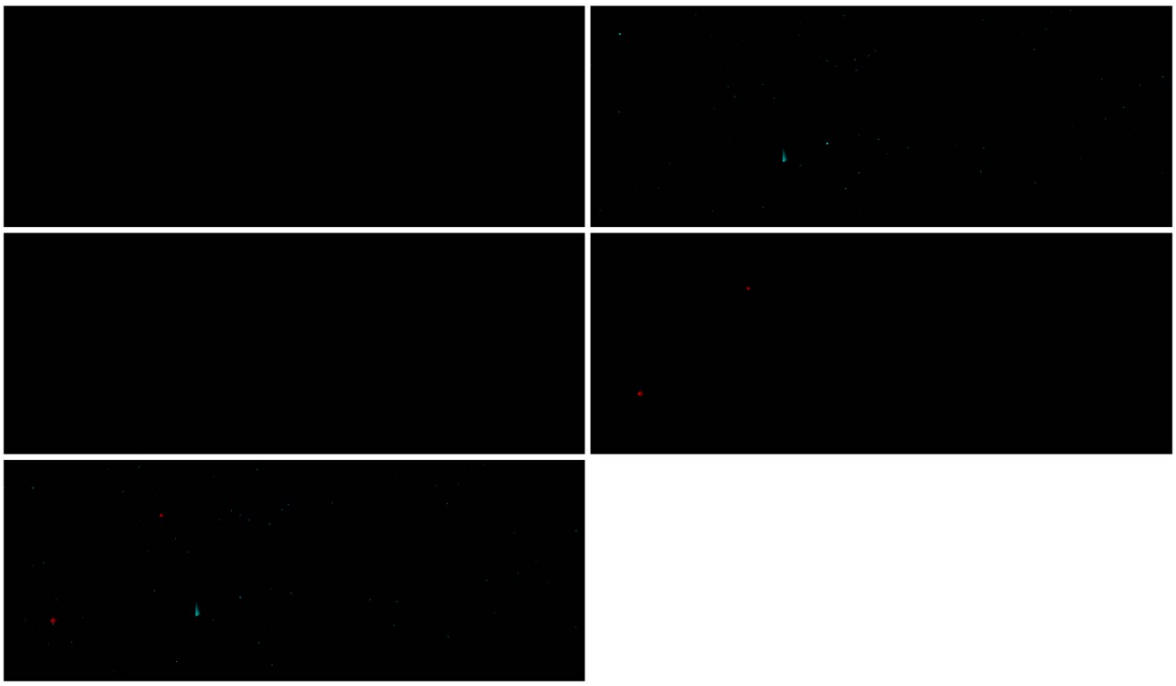

Figure S18: ToF-SIMS reconstructed ion images (90 µm x 30 µm) of TiO_2 NM-104 NMs agglomerates of different chemical entities from DMEM from an area where no agglomerate concentrations were observed; green: TiO_2 NM (NM-104) (a), blue: $TiOH^+$-serine (b); purple: $TiOH^+$ -leucine (c); red: $TiOH^+$ -phenylalanine (d); (e) shows an overlay of all ions. In the overlay picture, all chemical entities are separated from each other and do not co-localize.

[1] L.S. Sigg, W., Aquatische Chemie, Verlag der Fachvereine, Zürich, 1989.

[2] T. Mazza, E. Barborini, P. Piseri, P. Milani, D. Cattaneo, A. Li Bassi, C.E. Bottani, C. Ducati, Raman spectroscopy characterization of TiO2 rutile nanocrystals, Phys Rev B 75(4) (2007).

[3] Z. Movasaghi, S. Rehman, I.U. Rehman, Raman spectroscopy of biological tissues, Appl Spectrosc Rev 42(5) (2007) 493-541.

[4] Y.L. Zhao, C.H. Wang, Y. Zhai, R.Q. Zhang, M.A. Van Hove, Selective adsorption of L-serine functional groups on the anatase TiO2(101) surface in benthic microbial fuel cells, Phys Chem Chem Phys 16(38) (2014) 20806-20817.

[5] A.G. Thomas, W.R. Flavell, C.P. Chatwin, A.R. Kumarasinghe, S.M. Rayner, P.F. Kirkham, D. Tsoutsou, T.K. Johal, S. Patel, Adsorption of phenylalanine on single crystal rutile TiO2(110) surface, Surf Sci 601(18) (2007) 3828-3832.